MULTIPOINT ADJOINT SHAPE OPTIMIZATION OF A DIFFUSER VANE WITH OPEN-SOURCE SOFTWARE SU2

A Thesis

by

Lorenzo Fabris

Submitted to the

Graduate School of Sciences and Engineering
In Partial Fulfillment of the Requirements for
the Degree of

Master of Science

in the
Department of Mechanical Engineering

Özyeğin University
June 2024

Copyright © 2024 by Lorenzo Fabris

MULTIPOINT ADJOINT SHAPE OPTIMIZATION OF A DIFFUSER VANE WITH OPEN-SOURCE SOFTWARE SU2

Approved by:

Asst. Prof. Altuğ M. Başol, Advisor,
Department of Mechanical Engineering
Özyeğin Universitesi

Assoc. Prof. Özgur Ertunç,
Department of Mechanical Engineering
Özyeğin Universitesi

Assoc. Prof. Matteo Pini,
Chair of Propulsion and Power
Technische Universiteit Delft

Date Approved:

To the people who always believed in me, even when I did not.

ABSTRACT

Radial compressors equipped with vaned diffusers are widely used in industry. Vaned diffusers ensure higher pressure recovery compared to the vaneless diffusers. Specifically, the leading-edge shape of the vanes has large impact on the performance of the compressor. In this study the vaned diffuser geometry of a single radial compressor geometry is optimized using the discrete adjoint optimization technique. The optimization study was carried out with the open-source computational fluid dynamics software SU2 (Stanford University Unstructured). First, the optimization is performed for a single operating point of the compressor that is close to the choking conditions. Even though the optimized vane geometry performed considerably better at the choking conditions, the dramatic drop in the compressor performance at the operating point with the best efficiency showed the ineffectiveness of the optimization study focused only on a single operating point. Next, the optimization study was repeated using a multi-point optimization technique where the flow behavior at the two ends of the operating curve, one at the best efficiency point and the other close to the choking conditions, is considered. The study resulted in a performance increase along the whole operating range of the compressor where the rise in the compressor efficiency reached to about 2 % close to the choking conditions.

ÖZETÇE

Kanatlı difüzörlerle donatılmış radyal kompresörler endüstride yaygın olarak kullanılmaktadır. Kanatlı difüzörler, kanatsız difüzörlere göre daha yüksek basınç geri kazanımı sağlar. Spesifik olarak kanatların hücum kenarı kompresörün performansı üzerinde büyük etkiye sahiptir. Bu çalışmada, tek kademeli bir radyal kompresör geometrisinin kanatlı difüzör geometrisi, optimizasyon tekniği kullanılarak optimize edilmiştir. Optimizasyon çalışması açık kaynaklı hesaplamalı akışkanlar dinamiği yazılımı SU2 (Stanford University Unstructured) ile gerçekleştirilmiştir. Öncelikle kompresörün boğulma koşullarına yakın tek bir çalışma noktası için optimizasyon yapılmıştır. Optimize edilmiş kanat geometrisi boğulma koşullarında önemli ölçüde daha iyi performans gösterse de, en iyi verimliliğe sahip çalışma noktasında kompresör performansındaki dramatik düşüş, yalnızca tek bir çalışma noktasına odaklanan optimizasyon çalışmasının etkisizliğini göstermiştir. Daha sonra optimizasyon çalışması, biri en iyi verimlilik noktasında ve diğeri boğulma koşullarına yakın olan çalışma eğrisinin iki ucundaki akış davranışının dikkate alındığı çok noktalı optimizasyon tekniği kullanılarak tekrarlanmıştır. Çalışma, kompresörün tüm çalışma aralığı boyunca performans artışıyla sonuçlanmıştır. Kompresör verimliliğindeki artış, boğulma koşullarına yakın noktada yaklaşık %2'ye ulaşmıştır.

ACKNOWLEDGMENTS

The first moment I thought about my Master Thesis acknowledgments was immediately after deciding to commit myself to Academia. At the time, coming from a non-desirable experience during my Bachelor studies and a short – but extremely tough – entrepreneurial adventure, I was not able to foresee the incredible path waiting for me. It was my purgatory, it was my boulder to push to the top of the mountain. I owed it to myself for all the times I thought I could not make it because this was not the right path for me.

Regardless, I knew I would have wanted to deeply thank the people that not only supported me, but also joined this experience. I hope the next lines, here below, will show how grateful I am.

Firstly, I would like to thank Asst. Prof. Altug M. Basol for his incredible attitude and passion he provided during my studies in Ozyegin University, for the countless hours we spent discussing my results and the key points of our research, for his ability to not only be a great lecturer but also a supportive figure during my graduate studies and – most importantly – for the chance he took when he decided I was the right person for the project presented in this thesis.

To Assoc. Prof. Ozgur Ertunc I am extremely grateful for all the precious advices he was always ready to give, for the interesting lectures and discussions on fluid mechanics and for his great kindness.

Secondly, I would like to thank Dr. Bob C. Mischo, Dr. Sebastiano Mauri and Dr. Philipp Jenny – from MAN Energy Solutions Schweiz AG – for their great contribution to my research. Their efforts and knowledge were of key importance for my personal and professional growth.

Then, I would like to thank my friends Alvise, Mathias, Gianluca, Gabriele, Luca, Iheb, Paolo, Denis, Kutay, Aykan, Gizem and Gönül – scattered between Italy and Turkey – who always stood on my side during tough moments and difficult situations, things I will never forget. A small piece of this work is also theirs.

Moreover, I would like to thank Mehmet and Nisa: if my life in Turkey has been so easy, if I could adapt myself so well, it is because you welcomed me like a member of your family, always making me feel loved and appreciated.

Also, Ecem: you are the one who was there every day, who always understood me and that will always hold a place inside my soul. Without you I would not be here writing this thesis. I will not elaborate further to describe how I feel about this as any more words would be too many.

Finally, I want to thank my parents – Fabio and Sabrina – for their endless love and support, for investing their time and committing their lives so I could succeed and because, eventually, they never doubted about me. Even when I did.

The last paragraph of this section is dedicated to all the Italian students currently abroad, forced to leave their home country to get the chance to do what they love and follow their dreams while building their future. My wish is that, one day, our country will give us the same opportunities others are offering and we will not need to leave our families and friends to grant us a place in this world.

TABLE OF CONTENTS

LIST OF TABLES

LIST OF FIGURES

CHAPTER I

INTRODUCTION

The aim of turbomachinery research during the latest years has rapidly switched its focus on components optimization, given the increasing design requirements for future aero-engines and industrial plants. Moreover, a particular emphasis has been given to pollution and noise emissions reduction. While, in the past, turbomachinery optimization (turbines, compressors, fans and pumps) was carried out only relying on empirical correlation and charts – where the user's experience played a major role in the outcoming result and in the correct functioning of the device – nowadays the nimble development of computational resources lead to an increase in numerical methods reliability and utilization. However, designer's experience is still playing a key role being needed for the assessment of the final design output.

The advent of Computational Fluid Dynamics (CFD) in turbomachinery design baldly defines a watershed in shape optimization and design problems. The discretization of fluid domain and the use of numerical simulation make feasible the assessment of different designs in an extremely reduced time span, with the possibility of precisely defining the flow phenomena occurring in each of those, resulting in reduced costs for the industry.

From the late 1960s, CFD works developed from simple blade-blade throughflow models to 3D-analysis. During the last decade, it was possible to compute multi-stage unsteady analysis – with the application of different approaches (mixing plane or harmonic balance e.g.) – leading to extremely accurate definition of the flow phenomena in this type of machines. Please note that being the flow of turbomachines intrinsically unsteady, the interactions between each different component along the flow domain is, therefore, fundamental.

Furthermore, coupling CFD with numerical shape optimization is, arguably, one of the points of main interest, as it would results in an automatized design process. Shape optimization problems can be divided into different parts. Firstly, the aim of the optimization must be defined. This is generally done with the definition of the so called “objective function”. For instance, considering an externa flow over an airfoil, the objective function of a wing design problem could be drag minimization produced by the airfoil itself. Going back to the turbomachinery field, typical objective functions are averaged outlet total pressure – which will lead to the increase of the thermodynamic efficiency of the stage – or entropy generation minimization. Once the objective function is determined, the constraints must be defined: typically, turbomachines are fractions of larger industrial ste-ups, therefore extremely specific design requirements have been established in advance. A good example could be imposing constant mass flow rate along the passage. The main idea is that, rather than using experimental data to determine which part of the component desin is the most sensitive to flow quantities, the objective function value may now be determined using the direct solution provided by the aforementioned CFD solver.

To properly set up an optimization, a variety of techniques are used to minimize (or maximize) a specified objective function. These are typically characterized as stochastic, gradient-free or gradient-based metods. In the first, the optimizer attempts to reach a minimal value basing the optimization on the objective function’s derivative (or sensitivity). Nonetheless, the sucess rate of these kinds of approaches depends on the initial point selected and the dfinition of the optimization constraints. Because stochastic models require several flow solutions to converge, they might be prohibitively expensive for complex design problems including a greater number of parameters. As a result, the stochastic approach cannot be deemed appropriate for these kind of optimization problems.

To make the optimizer process the correct information, the gradient of the objective function needs to be calculated for each design step. This value can be computed using the finite difference method. Please not, though, that this operation will result in an additional computational cost, as each design variable requires the calculation of one flow solution. Again, this is constraining for turbomachinery applications since the number of design parameters involved in the calculations is, generally, quite consistent. Being its computational cost detached from the number of design variables chosen, the adjoint method has deviated from the previous appreaches, as more efficient way to calculate the objective function's gradient. However, even though its use is considerably common in external flow scenarios, discrete-adjoint applications for internal flows and turbomachinery problems have yet to be completely investigated.

Nonetheless, the gradients derived computed by the adjoint solver cannot be directly linked to the flow domain as the geometry is parametrized and its coordinates map eventually depends on differente variables. More precisely, two different sets of gradients are calculated: one for the underlying parametrization method and another for the adjoint solver. Both must be transferred to the optimizer after being "assembled". This operation determines the accuracy of the total gradient, so even though it is non-trivial, it is still fundamental.

Geometry must be correctly parametrized to have an efficient and optimization workflow. Moreover, a sufficient design space needs to be available for shape deformation. Generally, blade profile points on its surface are used as design variables. However, this leads to a huge number of control points that will negatively affect the computational cost of the operation, making impossible to obtain the expected result in a reasonable amount of time. Furthermore, constraints definition for the above-mentioned surface points is non-trivial and must be carried out by considering complex geometrical relationships. Also, without a further post-processing operation it would be impossible to evaluate the geometry as it will be presented as a cloud of surface points.

Based on what previously presented, the use of adjoint method is considered the most appropriate for the formulation of reliable and quick gradient-based optimization workflow and, therefore, utilized in the numerical work in this thesis.

As previously stated, due to the complex flow phenomena occurring in turbomachines and the high number of design variables present in turbomachinery shape design problems, the result is a time-consuming procedure for the optimization itself. Hence, the adjoint method was developed as a quick and efficient algorithm for these kind of optimization scenarios. Moreover, it is a well validated and exploited procedure for external flows optimization while it is not fully part of the optimization workflow for turbomachinery scenario. One of the critical features in gradient-based optimization of turbomachinery components is the multiple operating points the same design will be experiencing once implemented in an industrial setup. Specifically, the optimization of one single geometry with respect to a single operating point might affect the overall performance of the turbomachine, resulting in an inapplicable design for real uses. On the contrary, the possibility to perform gradient-based optimization ensuring that the overall efficiency will not be affected – if not positively – becomes the key for the utilization of this powerful tool.

Proceeding from this idea, the aim of this study is to present a steady, viscous, multi-point, gradient-based shape optimization for a three-dimensional, centrifugal compressor vaned diffuser flow scenario with the utilization of the discrete adjoint method.
Also, the flow field solutions will be computed with SU2 CFD open-source software. SU2 software was selected for three reasons:

1. It is an open-source software;
2. It already includes some specific, third part implemented modules that could make the optimization workflow smoother (discrete adjoint solver, mesh deformation algorithm e.g.)
3. Its solutions have been previously validated multiple times.

The workflow and the methodology are tested for a centrifugal compressor design optimization whose design is directly provided by MAN Energy Solutions Schweiz AG, which also validated the baseline flow field with its numerical, reference data. Specifically, the shape deformation will be applied to the vaned diffuser blade and its improvements or limitations will be deeply analyzed.

1.1 Turbomachinery: Theoretical Background

Turbomachinery refers to any device that uses the dynamics action of one or more blade rows to transfer energy to or from a continuosly flowing fluid. In particular, depending on the desired output of the machine itself, a rotor – a rotating row with blades installed

– or impeller applies a modification in the stagnation enthalpy of the fluid passing through it by exerting either positive or negative work on it. The physical feature that is directly connected to the fluid's pressure variation is this enthalpy change. However, the definition just mentioned it is extremely general and not sufficient for the purposes of this work (as it defines a wide range of turbomachines: fans, pumps, propellers e.g.).

Two main categories of turbomachines must be identified:

1. Absorbing power turbomachines, to increase the fluid pressure;
2. Producing power turbomachines, by expanding the fluid to a lower pressure.

By examining the characteristics of the flow path along the rotor, a categorization of turbomachines can also be carried out. The device is called an axial flow turbomachine if the flow path is entirely or mostly parallel to the rotational axis. A radial turbomachine is a device that has its flow path entirely in a plane normal to the rotational axis (Fig.1).

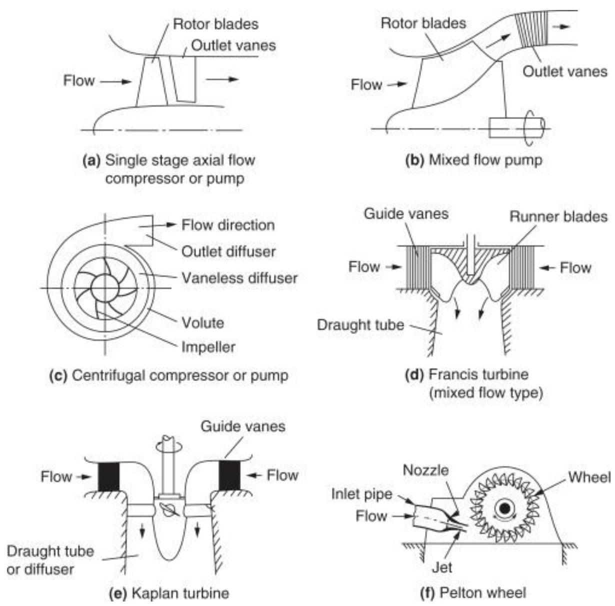

Figure 1: Different categories of turbomachines [1]

Please note that the mixed flow turbomachines category is referred to the direction of the flow at the rotor outlet when both radial and axial velocities are not negligible.

For completeness, another kind of turbomachinery categorization must be mentioned: all turbomachines might be classified as impulse or reaction machines with respect to pressure changes being present (or not) in the rotor. In an impulse device, all the pressure variations happen in the nozzle; subsequently the fluid is sent to the rotor (Fig.1, the Pelton wheel is an example of impulse turbine).

1.1.1 Performance Characteristics

If all the fluid velocities along the flow-passage domain are proportional to the blade speed and oriented in the same direction for any corresponding point, then the operating condition of a turbomachine will be dynamically similar at two different rotational velocities [1]. Iti is therefore reasonable to expect the latter to have th same numerical values for both points for the dimensionaless set of the parameters involved, neglecting Reynolds number effect. This explanation allows performance data to be represented non-dimensionally and condensed into a single curve (Fig.2).

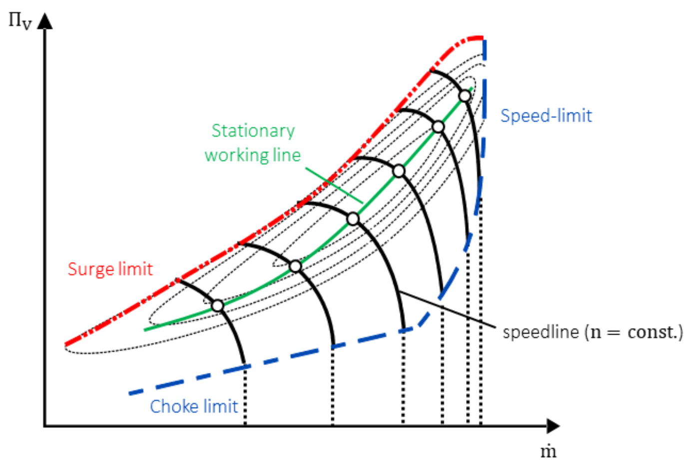

Figure 2: Characteristic performance map of a compressor.

Fig.2 represents the pressure ratio within the machine defined as function of $\dot{m}(\sqrt{T_{01}})/P_{01}$ for given values of $N/(\sqrt{T_{01}})$ [1]. Please note that subscript 1 is used to identify conditions at inlet. At first glance, it is possible to highlight the strong dependence of compressor performance with respect to $N/(\sqrt{T_{01}})$. Specifically for compressor, efficient operating points at constant $N/(\sqrt{T_{01}})$ can be found right beyond the surge line, which highlights the operating of a compressor (unstable operations are characteristically identified with great oscillation of the mass flow rate between inlet and outlet).

Choked regions, instead, are marked by the almost vertical segment of constant speedlines. Under these conditions no $\dot{m}(\sqrt{T_{01}})/P_{01}$ increase is feasible as Mach number reached the unity value in this section of the machine. Hence, the flow is choked.

1.1.2 Intrinsically Unsteadiness of Flow Scenarios in Turbomachinery

It is important to underline, for the correct consideration of the present work, that turbomachines perform the way they do due to unsteady effects occurring inside the flow domain. Given the mechanical interactions occurring on fluid particles in isentropic flows, the stagnation enthalpy change can only happen if the flow itself is unsteady. However, conditions for inlet and outlet regions are identified as steady.

In this work, only steady simulations were set up, occurring in an approximation based on the computational cost of the whole operations. How the accuracy of the solutions is affected will be treated in further chapters.

1.2 Fundamentals of Thermodynamics and Definition of Efficiency

In this section the basic principles of fluid mechanics and thermodynamics will be synthetically exposed and re-arranged to obtain relations useful for turbomachinery analysis and design. Numerical considerations that will be made further on in this work will be referring directly to this part of theoretical knowledge.

Specifically, the following relations will be derived and analyzed:

1. Continuity flow equation;
2. First Law of thermodynamics
3. Momentum equation
4. Second Law of thermodynamics and entropy definition
5. Isentropic and Polytropic efficiency definition.

Please note that the relationship mentioned here above are entirely generic and unaffected by whether the fluid is compressible or incompressible.

1.2.1 Continuity Equation

It is considered a fluid of given density ρ, flowing through the infinitesimal element of an area dA, in a specified time interval dT. If the stream velocity is defined as c, then the mass is $dm = \rho c \cdot \mathrm{d}t \cdot \mathrm{d}A \cdot \cos\theta$ where θ is the angle defined by the area of the element to the stream direction. The velocity component normal to the area $\mathrm{d}A$ is $c_n = c \cdot \cos\theta$ [1]. Hence $dm = \rho c_n \cdot \mathrm{d}t \cdot \mathrm{d}A$.

Consequently, the rate of mass flow is defined as follows:

$$d\dot{m} = \frac{dm}{dt} = \rho c_n \cdot \mathrm{d}A \tag{1.01}$$

1.2.2 First Law of Thermodynamics and Internal Energy

The first law of thermodynamics states that if a system is taken through a complete cycle during which heat is supplied and work is done, then:

$$\oint(dQ - dW) = 0 \tag{1.02}$$

where $\oint dQ$ stands for the head supplied to the system and $\oint dW$ stands for the work done by the system during the mentioned cycle [1].

While the change of state from 1 to 2 occurs, also the internal energy is subject to change:

$$E_1 - E_2 = \int_1^2 (dQ - dW) \quad (1.03)$$

If expressed in terms of an infinitesimal change of state, we can re arrange eq. 1.3 as follows:

$$dE = dQ - dW \quad (1.04)$$

For simplicity, the outcome of that derivation is reported below:

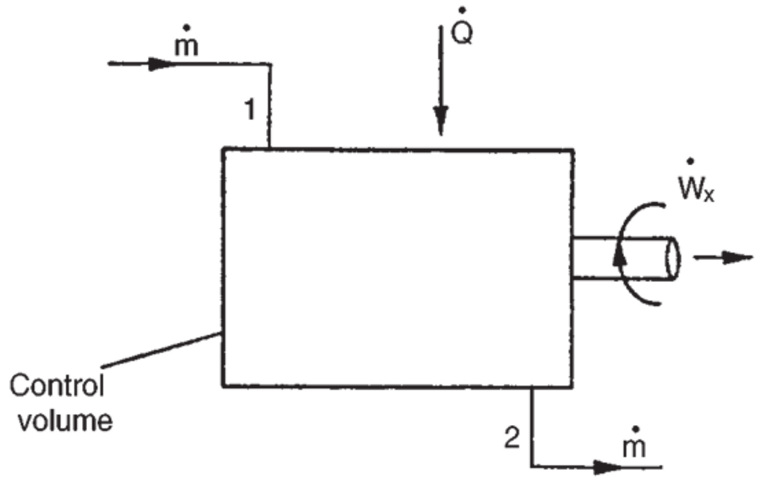

Figure 3: Control volume and sign convention for heat and work transfers [1]

Figure 3 shows the control volume selected to represent the turbomachine through which fluid passes at a constant rate of mass flow $\dot{m}$. The fluid flows from position 1 to position 2. Positive work is exerted on shaft at the rate $\dot{W}_x$ meaning that it is transferred from the fluid to the blades of the device. Generally, it is assumed positive the heat transfer $\dot{Q}$ when the heat flows from the environment to the control volume. Having established the sing convention, the steady flow energy equation is:

$$\dot{Q} - \dot{W}_x = \dot{m}\left[(h_2 - h_1) + \frac{1}{2}(c_2^2 - c_1^2) + g(z_2 - z_1)\right] \quad (1.05)$$

where h is the specific enthalpy, $\frac{1}{2}c^2$ is the kinetic energy per unit mass and gz the potential energy per unit mass [1].

Please note that last term's contribution in eq.1.5 is negligible except for hydraulic machines. Therefore, it is possible to define the stagnation enthalpy as $h_0 = h + \frac{1}{2}c^2$ and assume $g(z_2 - z_1)$ negligible. Consequently, eq.1.5 becomes:

$$\dot{Q} - \dot{W}_x = \dot{m}(h_{02} - h_{01}) \tag{1.06}$$

However, it is important to remember that most turbomachinery flow processes are adiabatic (or very close to it), this makes possible to define $\dot{Q} = 0$.

Eventually, the following relations are derived:

$$\dot{W}_x = \dot{W}_t = \dot{m}(h_{02} - h_{01}) \quad if\ \dot{W}_x > 0 \tag{1.07}$$

$$\dot{W}_c = -\dot{W}_x = \dot{m}(h_{02} - h_{01}) \ \ if\ \dot{W}_x < 0 \tag{1.08}$$

1.2.3 The momentum equation

The momentum equation relates the total external forces acting on a fluid element and its acceleration [1]. In the study turbomachines, an application of this relation can be well represented by the force exerted on a compressor or turbine blade due to the deflection or acceleration of the fluid flowing through the blades The time rate of change of the total x-momentum of a system of mass m is equal to the sum of all surface and body forces acting on the mass itself along the arbitrary x-direction [1],

$$\sum \boldsymbol{F_x} = \frac{\mathrm{d}}{\mathrm{d}\boldsymbol{t}}(\boldsymbol{mc_x}) \tag{1.09}$$

Hence, establishing a control volume that the fluid steadily crosses with inlet uniform velocity $\boldsymbol{c_{x1}}$ and outlet velocity of $\boldsymbol{c_{x2}}$ we can write what follows:

$$\sum \boldsymbol{F_x} = \dot{\boldsymbol{m}}(\boldsymbol{c_{x2}} - \boldsymbol{c_{x1}}) \tag{1.10}$$

Eq. 1.10 is the one-dimensional form of the steady flow momentum equation [1].

1.2.4 Entropy and second law of thermodynamics

The concept of entropy is introduced in several thermodynamic textbooks (e.g. Reynolds and Perkins, 1977) through the analysis of the second law of thermodynamics.

With respect to this, the Clausius inequality

$$\oint \frac{\mathrm{d}\boldsymbol{Q}}{\boldsymbol{T}} \leq \boldsymbol{0} \tag{1.11}$$

States that if all the processes in a heat exchange cycle are reversible, then $\mathrm{d}\boldsymbol{Q} = \mathrm{d}\boldsymbol{Q_R}$ and the equality stated in eq. 1.11 remains true for a system going through the cycle. In this case, $\mathrm{d}\boldsymbol{Q}$ is a fraction of heat transferred to the system at the absolute temperature $\boldsymbol{T}$.

The property called entropy, for a finite change of state, is defined as [1]

$$\boldsymbol{S_2} - \boldsymbol{S_1} = \int_{\boldsymbol{1}}^{\boldsymbol{2}} \frac{\mathrm{d}\boldsymbol{Q_r}}{\boldsymbol{T}} \tag{1.12}$$

Establishing a control volume through which the fluid steadily flows and experiences a change of state from condition 1 to condition 2, at inlet and outlet respectively, we have [1]:

$$\int_{\boldsymbol{1}}^{\boldsymbol{2}} \frac{\mathrm{d}\dot{\boldsymbol{Q}}}{\boldsymbol{T}} \leq \dot{\boldsymbol{m}}(\boldsymbol{S_2} - \boldsymbol{S_1}) \tag{1.13}$$

It is also possible to express the relation in eq.1.13 in terms of irreversibility:

$$\dot{\boldsymbol{m}}(\boldsymbol{S_2} - \boldsymbol{S_1}) = \int_{\boldsymbol{1}}^{\boldsymbol{2}} \frac{\mathrm{d}\dot{\boldsymbol{Q}}}{\boldsymbol{T}} + \boldsymbol{\Delta S_{irrev.}} \tag{1.14}$$

For an adiabatic process, $\mathrm{d}\dot{\boldsymbol{Q}} = \boldsymbol{0}$, then

$$S_2 \geq S_1$$

For reversible process, then

$$S_2 = S_1$$

Consequently, there will be no entropy variation (this kind of phenomena are called isentropic) for a flow undergoing a process that is isentropic. The best processes that can be carried out are an isentropic compression or expansion, given that turbomachinery is typically adiabatic, or close to these conditions. One of the main goals of any design is to minimize the irreversibility resulting from entropy generation in order to maximize the efficiency of a turbomachine.

When dealing with turbomachinery-related problems, entropy is especially helpful because it can be used to determine how much work and, consequently, machine efficiency has been lost as a result of an increase of entropy itself in the flow path. Moreover, the value of entropy is the same in absolute and relative frame of reference [1], meaning that the sources of inefficiency can be localized among all the stationary and rotating parts of the machine. A further discussion on entropy generation related to total pressure loss will be treated in the following chapters.

1.2.5 Compressor isentropic efficiency definition

The isentropic efficiency $\boldsymbol{\eta_c}$ of a compressor is generally defined as:

$$\eta_c = \frac{useful\ energy\ input\ to\ fluid\ unit\ in\ time}{power\ input\ to\ rotor}$$

The power supplied at the coupling is always more than the power input to the rotor (or impeller) because of the energy losses occurring in the bearings, glands, etc.

Therefore, the overall efficiency of compressor is:

$$\boldsymbol{\eta_0} = \frac{\boldsymbol{useful\ energy\ input\ to\ fluid\ unit\ in\ time}}{\boldsymbol{power\ input\ to\ coupling\ or\ shaft}}$$

Considering a complete adiabatic compression process from state 1 to state 2, the specific work input is [1]:

$$\boldsymbol{\Delta W_c = (h_{02} - h_{01}) + g(z_2 - z_1)}$$

In Fig.4, Mollier compression process is presented with a change of state 1–2 and its corresponding ideal process by 1–2s. Since potential energy changes are negligible in adiabatic compressor, the most meaningful efficiency is total-to-total efficiency, expressed as:

$$\boldsymbol{\eta_c = \frac{ideal\ work\ input}{actual\ work\ input} = \frac{h_{02s} - h_{01}}{h_{02} - h_{01}}} \tag{1.16}$$

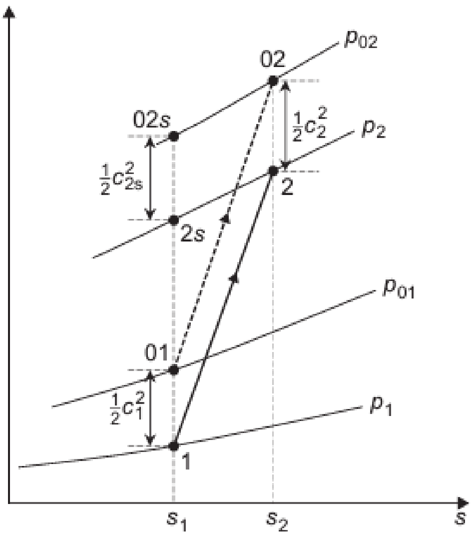

Figure 4: Adiabatic compression described in the Mollier's diagram [1].

A further simplification can be made if inlet and outlet kinetic energy quantities are not too diverse:

$$\boldsymbol{\eta_c = \frac{h_{2s} - h_1}{h_2 - h_1} = \frac{T_{2s} - T_1}{T_2 - T_1}} \tag{1.17}$$

1.2.6 Compressor polytropic efficiency definition

Though theoretically correct, the concept of isentropic efficiency as expounded in the preceding paragraph may be deceptive when evaluating the efficiency of turbomachines with different pressure ratios. Regardless of the device's actual number of stages, any turbomachine can be thought of as being composed of a large number of smaller stages. The isentropic efficiency of the machine will differ from the efficiency of the single small stages if every small stage has the same efficiency. This difference will depend on the machine's pressure ratio.

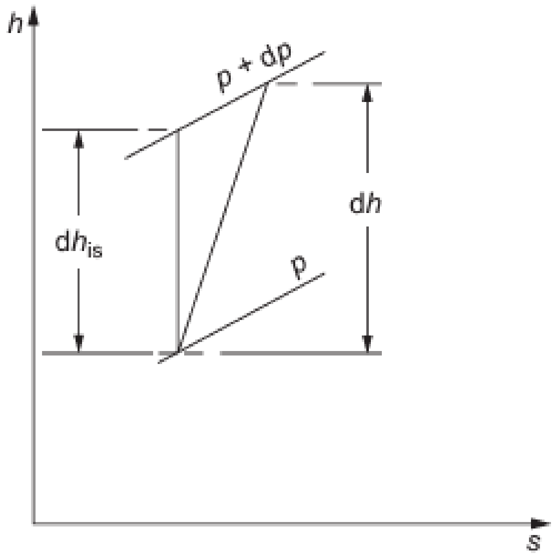

Figure 5: Incremental change of state in a compression process [1].

Considering a perfect gas in a small stage, an explicit relation can be derived for isentropic efficiency, small stage efficiency and pressure ratio.

The polytropic efficiency for a small stage is [1]

$$\boldsymbol{\eta_p} = \frac{\mathrm{d}\boldsymbol{h_{is}}}{\mathrm{d}\boldsymbol{h}} = \frac{\boldsymbol{v}\mathrm{d}\boldsymbol{p}}{\boldsymbol{C_p}\mathrm{d}\boldsymbol{T}} \tag{1.18}$$

Since for an isentropic process $\boldsymbol{T}\mathrm{d}\boldsymbol{s} = \mathbf{0} = \mathrm{d}\boldsymbol{h_{is}} - \boldsymbol{v}\mathrm{d}\boldsymbol{p}$.

Substituting $\boldsymbol{v} = \boldsymbol{RT}/\boldsymbol{p}$ into eq. 1.18 and defining $\boldsymbol{C_p} = \boldsymbol{\gamma R}/(\boldsymbol{\gamma} - \mathbf{1})$, the following is obtained:

$$\frac{\mathrm{d}\boldsymbol{T}}{\boldsymbol{T}} = \frac{(\boldsymbol{\gamma}-\mathbf{1})}{\boldsymbol{\gamma}\boldsymbol{\eta_p}}\frac{\mathrm{d}\boldsymbol{p}}{\boldsymbol{p}} \tag{1.19}$$

Integrating eq. 1.19 across the whole compressor and taking equal efficiency for each infinitesimal stage gives [1]:

$$\frac{\boldsymbol{T_2}}{\boldsymbol{T_1}} = \left(\frac{\boldsymbol{p_2}}{\boldsymbol{p_1}}\right)^{(\boldsymbol{\gamma}-\mathbf{1})/\boldsymbol{\eta_p}\boldsymbol{\gamma}} \tag{1.20}$$

Given the isentropic efficiency is expressed in eq. 1.17 for the ideal compression process $\boldsymbol{\eta_p} = \mathbf{1}$ is imposed in the same equation to obtain:

$$\frac{\boldsymbol{T_{2s}}}{\boldsymbol{T_1}} = \left(\frac{\boldsymbol{p_2}}{\boldsymbol{p_1}}\right)^{(\boldsymbol{\gamma}-\mathbf{1})/\boldsymbol{\gamma}} \tag{1.21}$$

Now, substituting eq. 1.20 and eq. 1.21 into eq. 1.18 the following expression is obtained:

$$\boldsymbol{\eta_c} = \frac{\left[\left(\frac{\boldsymbol{p_2}}{\boldsymbol{p_1}}\right)^{(\boldsymbol{\gamma}-\mathbf{1})/\boldsymbol{\gamma}} - \mathbf{1}\right]}{\left[\left(\frac{\boldsymbol{p_2}}{\boldsymbol{p_1}}\right)^{(\boldsymbol{\gamma}-\mathbf{1})/\boldsymbol{\eta_p}\boldsymbol{\gamma}} - \mathbf{1}\right]} \tag{1.22}$$

The small stage efficiency of a compression process is greater than the isentropic efficiency. The divergence of constant pressure lines determines this difference. Although this derivation was done for static state, stagnation state also obey to the same conditions as these values are related to static ones through isentropic processes.

CHAPTER II

NUMERICAL BACKGROUND

SU2 software suit was first developed in 2016 with the scope of solving partial differential equations (PDE) analyses and PDE-constrained optimization problems [2]. SU2 main feature is the Reynolds-Averaged Navier Stokes (RANS) solver effectively simulating the compressible, turbulent flows phenomena typically characterizing several problems in aerospace and mechanical engineering. Moreover, using the adjoint method, SU2 can provide gradient information that can be further utilized in shape optimization and adaptive mesh refinement. In this chapter, an assessment of turbomachinery optimization studies is carried out, deeply analyzing the numerical aspects of this matter. As specified in the introduction, this work is focused on gradient-based optimization. Particularly, the adjoint method is of great interest given its good adherence to the requirements dictated by the turbomachinery-related problems that will be further discussed in this chapter. The workflow for turbomachinery shape optimization problems can be represented as in Fig. 6:

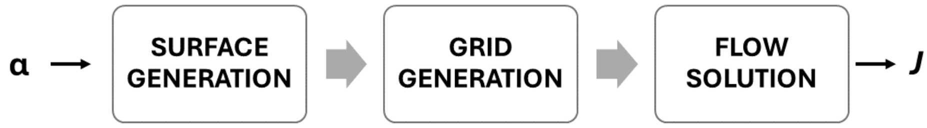

Figure 6: Aerodynamic shape optimization workflow in turbomachinery.

The core aspect of any shape optimization problem is the geometry parametrization. The geometry parametrizer utilized for this study will be described in section 2.1 of this chapter. Subsequently, the computational domain is discretized: for this study, the grid was generated by a third-party software for the baseline design and the existing mesh was deformed at the end of optimization loop. Eventually, the objective function is evaluated through the utilization of CFD.

Gradient-based numerical workflows need to comprehend how the objective function varies in relation to each design variable.

Eventually, section 2.4 will present an overview of some notable works that utilized the open-source CFD software SU2.

2.1 Shape parametrization techniques

Geometry parametrization is of key importance for the correct mesh deformation operated by the solver itself. Generally – regardless of the specific method used – the geometry parametrization technique is expected to be:

1. It must be fast.
2. It must be robust.
3. It must be efficient.
4. Able to reproduce the design space with a low number of design variables.

As shown by Anand et al. [3], an impact on the optimal solution is detected according to the type of parametrization modeling. In this work, a single parametrization technique is employed. However, two different methods can be identified:

- **CAD-free:** direct, or indirect. It is employed in this work.
- **CAD-based:** the geometry is parametrized with the use of Computer Aided Design.

Being the CAD-free approach the only one utilized in this study, the following section deeply describes its uses and characteristics.

2.2 CAD-free geometry parametrization

Three main techniques are presented in literature for both 2D and 3D:

- Node-based approach
- Analytical approach
- Free-form deformation.

In the following sections the differences between each approach are discussed and the choice for this study's geometry parametrization is explained.

2.2.1 Node-based approach

The coordinates of the surface grid nodes are utilized as design variables in the node-based (or discrete) approach. This can be regarded as one of the "richest" design spaces available as each node can be moved independently along the normal direction of either the curve (2D) or the surface (3D).

With respect to this matter, the work published by Wu and Liu [4], is arguably one of the first regarding the employment of a RANS-based adjoint method in turbomachinery shape design: the VKI turbine stator was optimized without any reference to geometrical constraints, as the latter were implemented directly in the objective function.

Nonetheless, the disadvantages of this technique, when utilized in aerodynamic shape optimization, are several and diverse:

- Complex penalty functions implementation based on the distance calculation in the fluid domain.
- Given the rich design space mentioned above, this might lead to meaningless shape deformation that requires the intervention of smoothing shape functions which are difficult to implement [5].
- The optimized shape needs an eventual transformation to industry-friendly formats (e.g. STEP) with related error in the mapping of the coordinates.

Having said that, the node-based approach cannot be deemed as suitable for the complexity intrinsically present in problems like the one presented in this work.

2.2.2 Analytical Approach

For this approach, similarly to what seen in the node-based method, shape functions are overlapped to the baseline design. These shape functions are smooth function modeled on a set of previous airfoil design [6]. In the literature, well established examples are Hicks-Henne or Radial Basis Functions (RBFs).

To modify the parameters defining the blade geometry, Duta et al. [7] used perturbation functions, where the main goal was to prove the functionality of Automatic Differentiation on the existing CFD code HYDRA [8] to later obtain its discrete adjoint solution. Specifically, NASA rotor 37 was the selected geometry for the test case.

Wang et al [9,10]., developed a treatment of the adjoint mixing-plane for multi-row turbomachinery test cases on steady RANS equations. Three compressors cases are studied in this work and the geometry of each of them is deformed with the utilization of Hicks-Henne functions.

However, the disadvantages of this method are rather shared with the node-based approach.

2.2.3 FFD-box Approach

For this approach, the blade is enclosed in a box formed by the control points that will be later moved to perform the shape deformation. The model can be conceptually visualized as a rubber being twisted, bent, expanded or compressed while its topology is preserved [6].

This technique is commonly used for wings shape deformation in optimization problems. However, especially for three-dimensional domains, its usage in turbomachinery optimization problem is rather uncommon. Anand et al [3]., performed an optimization of a 2D turbine blade profile by using FFD and the author clearly highlights the complexity of geometrical constraints definition. Furthermore, Vitale [11] uses FFD boxes to validate gradients from the discrete adjoint solver in the open source software SU2 [2]. As a result, entropy generation across the passage is minimized, however of maintaining the TE shape out of the FFD box to constrain the shape deformation in this region.

Being the design variables are also the control points, it is crucial to emphasize that the FFD-box does not permit direct control of the geometry deformation. This could result in unphysical geometries, particularly from a manufacturing standpoint. Furthermore, a significant influence on the shape deformation's outcome is the placement of the FFD-box itself.

However, even if CAD-free techniques might be non-trivial, in the context of this work test case scenario, the FFD-box approach was deemed adequate given the specific design of the region interested by the shape deformation, as will be treated in the respective chapter.

2.3 Computational Domain

The CFD solver needs a computational, unstructured, grid to compute the flow solution. This grid needs to be dense enough to accurately simulate all the complex flow behaviors occurring in a turbomachinery passage, with an important focus on the ones close to the blade surface where the boundary may separate due to adverse pressure gradients.

As design variables are directly responsible for the grid-points displacement, hence the shape will be different for each optimization loop carried out. Hence, the solver requires a volumetric mesh as input – that slightly differs from the one of the previous iterations – to perform a new evaluation of the flow solution. This mesh, while maintaining the same density and features of the baseline one, must be robust and capable of capturing the flow phenomena. Otherwise information can be lost during the optimization workflow.

For this study the mesh deformation approach was chosen and carried out imposing some constraints to avoid inconsistencies in the new computational domain.

2.3.1 Mesh deformation

Mesh deformation is the process that modifies the initial grid in each optimization step in accordance with the newly defined surface coordinates that the optimizer sets. Mesh creation is therefore only necessary at the very first stage of the optimization process. Most importantly, it is only required once.

RBFs, linear elasticity-based and spring-analogy methods are often used in the mesh deformation process. When using algorithms based on linear elasticity, the volumetric mesh as whole is regarded a linear elastic material, and the linear elasticity equations are subject to the unknown displacement as Dirichlet boundary conditions. When compared to spring-analogy, these algorithms can perform better on meshes with very high-aspect ratio with boundary layer refinement, as highlighted in Xu et al [12].

The utilization of mesh deformation algorithms allows for a major saving in terms of computational cost. However, to ensure stable results, the mesh deformation process must be characterized by a good robustness. It is noted from the literature that this step is often disregarded and only treated carefully in some works [12]. Regardless, the hub and shroud surfaces receive no particular attention in the literature review. However, this might lead to some issues during the grid generation phase as these surfaces are susceptible to blade movement, which may change the gradients computed by the adjoint solver as well as the mass flow through the passage.

In the end, it is found that re-meshing works best in situations where there are quick, reliable and effective in-house grid generators available, as these provide for considerable geometry control. This is a computationally demanding task that could result in information loss during the optimization process. Being this the case where grid quality in critical regions of the grid is maintained high, the mesh deformation approach was chosen to carry out this study.

2.4 Adjoint method

While performing adjoint optimizations, the sensitivities – relative to the defined objective function – must be computed in a way such that the optimizer gathers enough information to correctly converge to the next design iteration, eventually moving towards the final optimized design.

In turbomachinery adjoint optimization set-ups, where the underlying surface parametrization is expressed as $\boldsymbol{X_{surf}} = \boldsymbol{X_{surf}}(\boldsymbol{\alpha})$, the objective function can be written as

$$\boldsymbol{J} = \boldsymbol{J}(\boldsymbol{x}, \boldsymbol{\alpha}) \tag{2.01}$$

where

$$\boldsymbol{X} = \boldsymbol{X}(\boldsymbol{X_{surf}}(\boldsymbol{\alpha})) \tag{2.02}$$

Consequently, the total gradient of $\boldsymbol{J}$, given its design variables $\boldsymbol{\alpha}$ is if the chain rule is applied to eq. 2.02:

$$\frac{\mathrm{d}\boldsymbol{J}}{\mathrm{d}\boldsymbol{\alpha}} = \frac{\mathrm{d}\boldsymbol{J}}{\mathrm{d}\boldsymbol{x}}\, \frac{\mathrm{dX}}{\mathrm{d}\boldsymbol{X_{surf}}}\, \frac{\mathrm{d}\boldsymbol{X_{surf}}}{\mathrm{d}\boldsymbol{\alpha}}. \tag{2.03}$$

Generally, adjoint solvers are implemented and integrated in existing CFD software's suite (e.g. HYDRA [8], OpenFOAM [13], ANSYS Fluent [14] or SU2 [2]).

The second term, corresponding to the mesh sensitivity, is computed by the adjoint solver but it can be calculated also by finite differences (FD) [15]. The dot product between the adjoint solution and the mesh sensitivities is necessary to project the volumetric sensitivities onto the surface to be deformed, $\frac{dJ}{\mathrm{d}\boldsymbol{X_{surf}}}$.

Eventually, the last term – corresponding to the surface sensitivities – can be computed in different ways: finite differences, using the complex-step method [16] or by differentiation of the underlying parametrization method. This procedure is generally carried out with the implementation of algorithmic differentiation (AD). This technique is particularly effective because it returns the exact gradient even though the implementation is non-trivial.

The adjoint method was successfully proven effective in the past decades due to its quick gradient computation of the objective function with respect to design variables. It was firstly developed by Jameson from the control theory utilization in aerodynamics application [17] and it grants the objective function gradient calculation independently from the number of design variables. Given these considerations, it is deduced that the discrete-adjoint approach particularly fits for turbomachinery design problems, where a huge number of design variables calls for quick computational time in complex industrial applications.

Table 1: Type of gradients to compute necessary for the objective function sensitivity calculation.

Name	Symbol	Obtained by
Objective sensitivity	$\frac{\mathrm{d}\boldsymbol{J}}{\mathrm{d}\boldsymbol{x}}$	Adjoint solver
Mesh Sensitivity	$\frac{\mathrm{d}\mathbf{X}}{\mathrm{d}\boldsymbol{X}_{surf}}$	FD mesh deformation AD mesh deformation
Surface Sensitivity	$\frac{\mathrm{d}\boldsymbol{X}_{surf}}{\mathrm{d}\boldsymbol{\alpha}}$	FD geom. parametrizer AD geom. parametrizer

Two types of approach can be followed when operating with the adjoint method: continuous or discrete. In continuous adjoint the equations are derived from the linearized flow equations. Moreover, as shown by Papadimitriou and Giannakoglou [18], the sensitivity of the interior grid nodes coordinates with respect to the design variables does not need to be computed being the adjoint equations derived without field terms.

Discrete approach, instead, is computationally more expensive but it computes the exact gradient of the objective function, allowing an efficient and safe convergency rate of the solver [19] that makes it well suited for complex design problems.

2.5 Shape optimization in SU2

Having discussed all the components of the optimization problem, it is now fundamental to define the performances of the CFD suite chosen for this study: SU2.

Firstly, SU2 was developed with a focus on external flow applications, with good capabilities for sensitivity prediction using both continuous and adjoint solver. Moreover, the software contains a mesh deformation algorithm that, when coupled with the adjoint solver, makes SU2 a complete framework for gradient-based optimization [2].

Recently, SU2 has been further developed with a focus on internal flows with particular attention to turbomachinery features such as non-reflecting boundary conditions. Also, the possibility of computing unsteady optimization was implemented within the code using harmonic-balance technique [11, 20].

In the aforementioned works, discrete adjoint gradients were validated for different axial and centrifugal test cases with a complete optimization study on the 3D Aachen turbine geometry [11] using the FFD box shape parametrization.

Nonetheless, SU2 adjoint optimization capabilities for radial compressors test cases and for multipoint set ups are yet to be fully investigated. Hence, the focus of this work will be on:

- The use of SU2 for radial compressor test cases flow field validation with respect to the reference speed line.
- The numerical evaluation of the optimized shape.

CHAPTER III

NUMERICAL METHODOLOGY

The methodology that allows the implementation of the process chain necessary for the multi-point optimization of radial turbomachinery is thoroughly analyzed.

In section 3.1 the workflow for adjoint-based problem is presented. Sections 3.2 will discuss the shape parametrization and mesh deformation algorithm. Subsequently, SU2 flow and adjoint solver will be described in section 3.3. The final section will discuss the optimization problem definition.

3.1 Workflow

In chapter 2 how the optimization problem is composed of different modules was already discussed. These modules perform the operations that necessary to compute two main features that the solver will use to converge to the optimized shape:

- Objective function $\boldsymbol{J}$
- Gradient of the objective function with respect to the design variables.

Firstly, geometry is parametrized with the use of the design variables. These will subsequently generate the ensemble of the surface grid coordinates X_{surf}. The updated surface coordinates will constitute the input for the grid deformation algorithm, that will output the modified volume mesh **X.** The flow solution is computed by the flow solver, consequently the objective function J is calculated.

A schematic representation of this process can be visualized as follows:

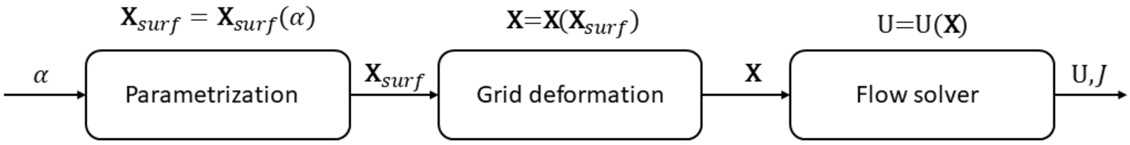

Figure 7: Flow chart describing the objective function calculation.

Similarly, Fig.8 displays the total sensitivity calculation flow chart for this kind of problem. Specifically, the three modules are called independently, resulting in the generation of three different sensitivities.

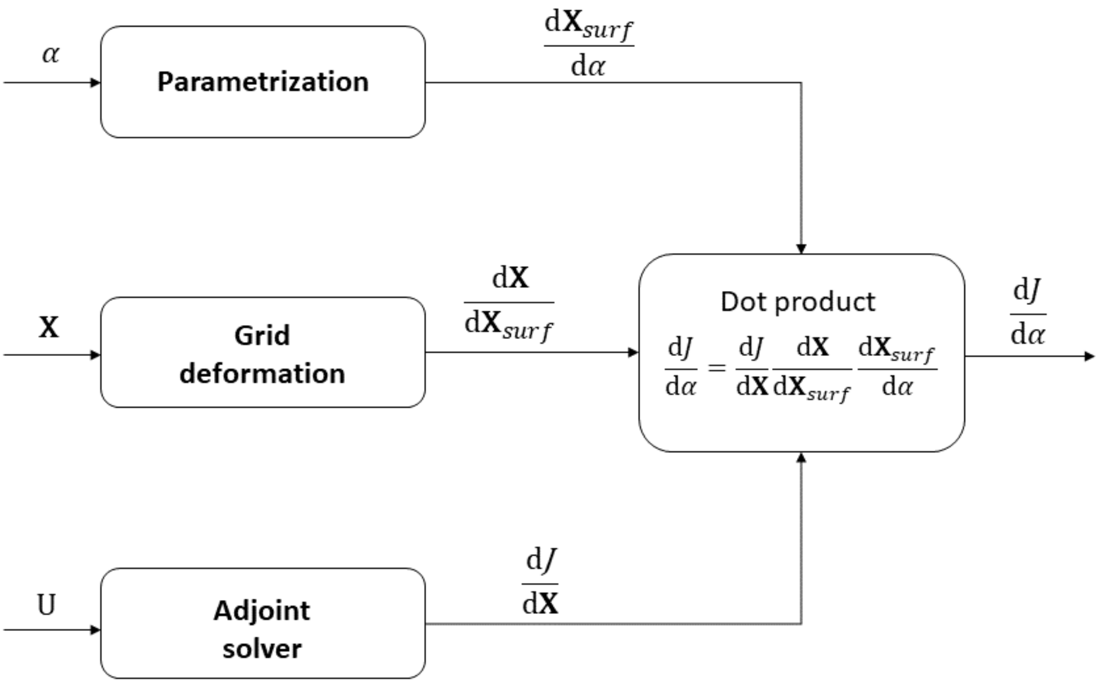

Figure 8: Schematic flow chart for total sensitivities computation.

3.2 Surface parametrization

As discussed in chapter 2, the surface parametrization chosen for this study is a CAD-free, FFD box approach. While this approach could be weakened in the presence of a huge number of design variables, in the further chapters – where the actual optimization study will be described – some constraints to the design variable's location variation will be applied, allowing this method to converge properly.

3.2.1 Surface sensitivities

As described by eq. 2.03, to compute the total objective function sensitivities, the geometrical sensitivities – described by $\frac{\mathrm{d}\mathbf{X}_{\mathrm{surf}}}{\mathrm{d}\alpha}$ – should be computed in advance. This way, it is possible to understand how the surface points are displaced with a manipulation of the design variables. The sensitivities aforementioned can be calculated in different ways:

- Finite difference: the design variables α define the surface coordinates $\mathbf{X}_{surf}$. Thus, a deformation step δ is defined as the perturbation magnitude of the design variables. Subsequently, the geometrical gradient can be computed with the well-known finite difference method as follows:

$$\frac{\mathrm{d}\mathbf{X}_{\mathrm{surf}}}{\mathrm{d}\alpha} \approx \frac{\mathbf{X}_{surf}(\alpha+\delta)-\mathbf{X}_{surf}(\alpha)}{\delta} \tag{3.01}$$

if a forward scheme is used, or as

$$\frac{\mathrm{d}\mathbf{X}_{\mathrm{surf}}}{\mathrm{d}\alpha} \approx \frac{\mathbf{X}_{surf}(\alpha+\delta)-\mathbf{X}_{surf}(\alpha-\delta)}{2\delta} \tag{3.02}$$

- Complex-step: in the complex-step method [16] the surface generation algorithm receives an imaginary step input defined as $\mathbf{X}_{surf} = \mathbf{X}_{surf}(\alpha + i \cdot \delta)$. The surface points imaginary part is then used to compute the first derivative of the objective function,

$$\frac{\mathrm{d}\mathbf{X}_{\mathrm{surf}}}{\mathrm{d}\alpha} \approx \frac{1}{\delta}\mathrm{Im}\left[\mathbf{X}_{surf}(\alpha + i \cdot \delta)\right] \tag{3.03}$$

3.2.2 Mesh deformation

The optimizer computes the displacement associated with this deformation generating the new set of blade coordinates. Mesh deformation is firstly achieved by moving the surface boundary. Subsequently, the volumetric deformation is carried out, based on the classical spring-analogy method [21].

The system of equations to be solved in order to obtain the new volumetric grid displacement is [2]

$$\left(\sum_{j \in \mathbb{N}(i)} \boldsymbol{k_{ij} e_{ij} e_{ij}^T}\right)\boldsymbol{u_i} = \sum_{j \in \mathbb{N}(i)} \boldsymbol{k_{ij} e_{ij} e_{ij}^T u_j} \tag{3.04}$$

where $\boldsymbol{k_{ij}}$ is the stiffness matrix, $\mathbb{N}(\boldsymbol{i})$ is the set of neighboring points to node $\boldsymbol{i}$ and $\boldsymbol{e_{ij}}$ is the unit vector connecting both points. The spring-analogy grid deformation algorithm is already implemented in SU2 suite, specifically within the SU2_DEF module. Several options can be set up to smooth the mesh deformation process:

- Wall distance: stiffest elements close to the endwalls

$$\boldsymbol{E} \propto \frac{\boldsymbol{1}}{\boldsymbol{wall\ distance}}. \tag{3.05}$$

- Inverse volume: stiffest elements are the ones, smallest volume (e.g. boundary layer refinement mesh)

$$\boldsymbol{E} \propto \frac{\boldsymbol{1}}{\boldsymbol{element\ volume}}. \tag{3.06}$$

- Constant stiffness: constant Young’s modulus, $\boldsymbol{E} = \boldsymbol{E_0}$

The boundary layer refinement, highly linked to the above-mentioned type of stiffness, directly affects the mesh deformation process chain, as well as the volume grid deformation.

- Poisson's ratio: the ratio of the transverse contraction strain to the longitudinal extension strain in the direction of the stretching force. It is useful to control the locking of the mesh elements.

3.2.3 Mesh sensitivities

The objective function's gradient computation calls for the mesh sensitivities (eq. 2.03) $\frac{\mathrm{d}\mathbf{X}}{\mathrm{d}\mathbf{X}_{surf}}$.

The spring-analogy deformation tool makes use of the automatic differentiation to calculate this value. Specifically to SU2, this passage is executed by a different module called SU2_DOT_AD, that produces a map of mesh sensitivities as follows:

$$\frac{\mathrm{d}\mathbf{X}}{\mathrm{d}\boldsymbol{X}_{surf}} = \left(\frac{\partial x}{\partial \mathrm{X}_{surf}}, \frac{\partial y}{\partial \mathrm{X}_{surf}}, \frac{\partial z}{\partial \mathrm{X}_{surf}}\right) \tag{3.07}$$

3.3 Flow and adjoint solver

Open-source suite SU2 [2], is used as flow (SU2_CFD) and discrete adjoint (SU2_CFD_AD) solver. SU2 modules used in this study are described in the following sections.

3.3.1 Flow solver

Euler and RANS solvers are both implemented in the CFD tool available in SU2. In this work, the focus is on the RANS solver, given that turbulence and other viscous phenomena are not negligible in turbomachinery scenarios. However, when solving

RANS equations, the turbulence must be analytically defined for the problem to be solved. SU2 includes both Spalart-Allmaras [22] and k-ω SST [23] turbulence models.

Finite Volume Method (FVM) is used to discretize the PDEs. Central and upwind schemes are both available for the discretization of convective fluxes (e.g. JST [24] or Roe [25]). For high-order upwind schemes, limiters are available, e.g. Venkatakrishnan [26] and Van Albada [27]. For the flow field simulation RANS solver was selected. RANS equations in SU2 are discretized through and implementation of the finite volume method with a standard edge-based structure on a dual grid with control volumes that are built using a medial-dual vertex-based scheme [2]. The semi-discretized integral form of the method's governing equation is:

$$\int \frac{\partial \boldsymbol{U}}{\partial t} d\Omega + \sum_{j \in \mathbb{N}(i)} \left(\widetilde{\boldsymbol{F}_{ij}^{c}} + \widetilde{\boldsymbol{F}_{ij}^{v}} \right) \Delta S_{ij} - \boldsymbol{Q} |\Omega_i| = \int \frac{\partial \boldsymbol{U}}{\partial t} d\Omega + \boldsymbol{R_i}(\boldsymbol{U}) = 0 \qquad (3.08)$$

where $\boldsymbol{R_i}(\boldsymbol{U})$ is the residual vector resulting from the integration of the source term over the control volume Ω_i and the sum of all the projected convective and viscous fluxes $\widetilde{\boldsymbol{F}_{ij}^{c}}$ and $\boldsymbol{F}_{ij}^{v}$, the residual is computed for each inner and boundary node, respectively. Detailed description of the implementation of this discretization in SU2 can be found in Economon et Al [2].

3.3.1.1 Time discretization

Time discretization is carried out by the solver with the utilization of an implicit Euler scheme – after the calculation of the residual vector – originating the following linear system:

$$\left(\frac{|\Omega|}{\Delta t^n} + \frac{\partial \boldsymbol{R}(\boldsymbol{U}^n)}{\partial \boldsymbol{U}^n} \right)_J \Delta \boldsymbol{U}_J^n = -\boldsymbol{R}(\boldsymbol{U}^n) \qquad (3.09)$$

where $\Delta \boldsymbol{U}^n := \boldsymbol{U}^{n+1} - \boldsymbol{U}^n$ and t^n is the (pseudo) time step. The numerical implementation of this time discretization method can be found in Vitale et al, 2020 [28].

3.3.1.2 Boundary Conditions

With respect to the problem setting, different type of boundary conditions can be selected:

- No-slip adiabatic wall
- Symmetry walls
- Periodic Interfaces
- Non-reflecting boundary condtions for different surfaces (e.g. inlet, outlet, mixing-plane)

The specific settings for the test case will be discussed in the relative chapter of this work.

3.3.2 Adjoint Solver

SU2 is implemented with both continuous and discrete approach when it comes to adjoint solver. Due to the advantages described in Chapter 2, this work will be focusing on discrete adjoint approach. Algorithmic Differentiation is the tool that allows the computation of the adjoint solution in SU2 suite by calculating the differentiation of the primal solver. This operation is carried out in SU2_CFD_AD module.

3.3.3 Adjoint Sensitivities

The scalar objective function $\boldsymbol{J}$, it is a function of the flow vector $\mathbf{U}$ and the mesh points $\mathbf{X}$ for aerodynamic shape optimization problem. It is possible to express $\boldsymbol{J}$ with respect to its design variables as follows:

$$\boldsymbol{J} = \boldsymbol{J}(\mathbf{U}(\boldsymbol{\alpha}), \mathbf{X}(\boldsymbol{\alpha})) \tag{3.10}$$

Generally, the objective function is minimized while the whole problem set up obeying to the following:

$$\mathbf{U} = \mathbf{G}(\mathbf{U}, \mathbf{X}) \tag{3.11}$$

$$\mathbf{X} = \mathbf{M}(\boldsymbol{\alpha}) = \boldsymbol{V}\big(\boldsymbol{S}(\boldsymbol{\alpha})\big) \tag{3.12}$$

The adjoint equation is consequently derived by the use of the Lagrangian approach:

$$L(\boldsymbol{\alpha}, \mathbf{U}, \mathbf{X}, \overline{\mathbf{U}}, \overline{\mathbf{X}}) = \mathrm{J}(\mathbf{U}, \mathbf{X}) + [\mathbf{G}(\mathbf{U}, \mathbf{X}) - \mathbf{U}]^{\mathrm{T}}\overline{\mathbf{U}} + [\mathbf{M}(\boldsymbol{\alpha}) - \mathbf{X}]^{\mathrm{T}}\overline{\mathbf{X}} \tag{3.13}$$

Since the derivative of L with respect to α is obtained, and $\overline{\mathbf{U}}$ and $\overline{\mathbf{X}}$ are selected in such a way that the computationally expensive terms $\frac{\partial \mathrm{U}}{\partial \alpha}$ and $\frac{\partial \mathrm{X}}{\partial \alpha}$ are eliminated, this gives what follows:

$$\overline{\mathbf{U}} = \frac{\partial}{\partial \mathbf{U}} J^{T}(\mathbf{U},\mathbf{X}) + \frac{\partial}{\partial \mathbf{U}} \mathbf{G}^{T}(\mathbf{U},\mathbf{X})\overline{\mathbf{U}} \tag{3.14}$$

$$\overline{\mathbf{U}} = \frac{\partial}{\partial \mathbf{X}} J^{T}(\mathbf{U},\mathbf{X}) + \frac{\partial}{\partial \mathbf{X}} \mathbf{G}^{T}(\mathbf{U},\mathbf{X})\overline{\mathbf{U}} \tag{3.15}$$

Eq. 3.14 and 3.15, respectively, correspond to the adjoint and mesh sensitivity.

Hence, using eq. 3.15 it is possible to compute the mesh sensitivities after the adjoint solution is computed. The total derivative of thje objective function can be expressed as:

$$\frac{\mathrm{d}J^{T}}{\mathrm{d}\alpha} = \frac{\mathrm{d}}{\mathrm{d}\alpha} \mathbf{M}^{T}(\alpha)\overline{\mathbf{X}} \tag{3.16}$$

where

$$\frac{\mathrm{d}\mathbf{M}}{\mathrm{d}\alpha} = \frac{\mathrm{d}\mathbf{X}}{\mathrm{d}\mathbf{X}_{surf}} \frac{\mathrm{d}\mathbf{X}_{surf}}{\mathrm{d}\alpha} \tag{3.17}$$

It is of relevant importance the fact that, while operating with SU2 software, only the computation performed by SU2_CFD_AD and SU2_DOT_AD will return the objective function sensitivities for the blade surface:

$$\frac{\mathrm{d}J}{\mathrm{d}\mathrm{X}_{surf}} = \left(\frac{\partial J}{\partial \mathrm{x}_{surf}}, \frac{\partial J}{\partial \mathrm{y}_{surf}}, \frac{\partial J}{\partial \mathrm{z}_{surf}}\right) \tag{3.18}$$

3.4 Total gradient calculation

The overall derivative (or sensitivity) of the objective function must be assembled after the gradient information is available from the design chain described in Fig.7. The calculation of the total gradient can be better explained with an example.

A 2D section of a turbine blade is considered (Fig.9) and a trivial parametrization is applied to its profile: single design variable controls the location of three random points on the blade profile.

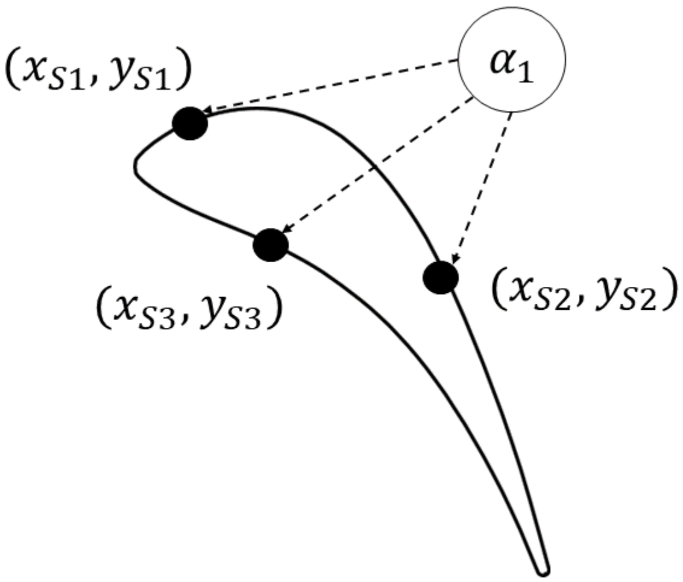

Figure 9: Turbine blade section basic parametrization.

The objective function's gradient it is a matrix of sensitivities presented as follows:

$$\frac{\mathrm{d}\boldsymbol{J}}{\mathrm{dX}_{\boldsymbol{surf}}} = \begin{pmatrix} \frac{\partial \boldsymbol{J}}{\partial \boldsymbol{x_{S1}}} & \frac{\partial \boldsymbol{J}}{\partial \boldsymbol{y_{S1}}} \\ \frac{\partial \boldsymbol{J}}{\partial \boldsymbol{x_{S2}}} & \frac{\partial \boldsymbol{J}}{\partial \boldsymbol{y_{S2}}} \\ \frac{\partial \boldsymbol{J}}{\partial \boldsymbol{x_{S3}}} & \frac{\partial \boldsymbol{J}}{\partial \boldsymbol{x_{S3}}} \end{pmatrix} \tag{3.19}$$

The parametrization sensitivities will be:

$$\frac{\mathrm{dX}_{\boldsymbol{surf}}}{\mathrm{d}\boldsymbol{\alpha_1}} = \begin{pmatrix} \frac{\partial \boldsymbol{x_{S1}}}{\partial \boldsymbol{\alpha_1}} & \frac{\partial \boldsymbol{y_{S1}}}{\partial \boldsymbol{\alpha_1}} \\ \frac{\partial \boldsymbol{x_{S2}}}{\partial \boldsymbol{\alpha_1}} & \frac{\partial \boldsymbol{x_{S2}}}{\partial \boldsymbol{\alpha_1}} \\ \frac{\partial \boldsymbol{x_{S3}}}{\partial \boldsymbol{\alpha_1}} & \frac{\partial \boldsymbol{x_{S3}}}{\partial \boldsymbol{\alpha_1}} \end{pmatrix} \tag{3.20}$$

According to eq.2.03, the total sensitivities are equal to the inner product of both sensitivity maps:

$$\frac{\mathrm{d}\boldsymbol{J}}{\mathrm{d}\boldsymbol{\alpha_1}} = \left(\frac{\mathrm{d}\boldsymbol{J}}{\mathrm{dX}_{\boldsymbol{surf}}}\right)\left(\frac{\boldsymbol{dX_{surf}}}{\boldsymbol{d\alpha_1}}\right)^{\boldsymbol{T}} = \begin{pmatrix} \frac{\partial \boldsymbol{J}}{\partial \boldsymbol{x_{S1}}} & \frac{\partial \boldsymbol{J}}{\partial \boldsymbol{y_{S1}}} \\ \frac{\partial \boldsymbol{J}}{\partial \boldsymbol{x_{S2}}} & \frac{\partial \boldsymbol{J}}{\partial \boldsymbol{y_{S2}}} \\ \frac{\partial \boldsymbol{J}}{\partial \boldsymbol{x_{S3}}} & \frac{\partial \boldsymbol{J}}{\partial \boldsymbol{x_{S3}}} \end{pmatrix} \begin{pmatrix} \frac{\partial \boldsymbol{x_{S1}}}{\partial \boldsymbol{\alpha_1}} & \frac{\partial \boldsymbol{x_{S2}}}{\partial \boldsymbol{\alpha_1}} & \frac{\partial \boldsymbol{x_{S3}}}{\partial \boldsymbol{\alpha_1}} \\ \frac{\partial \boldsymbol{y_{S1}}}{\partial \boldsymbol{\alpha_1}} & \frac{\partial \boldsymbol{x_{S2}}}{\partial \boldsymbol{\alpha_1}} & \frac{\partial \boldsymbol{x_{S3}}}{\partial \boldsymbol{\alpha_1}} \end{pmatrix} \tag{3.21}$$

Eq. 3.21 can be re-arranged in a more general form, for three-dimensional cases with more than one design variable as follows:

$$\frac{\mathrm{d}\boldsymbol{J}}{\mathrm{d}\boldsymbol{\alpha_1}} = \sum_{\boldsymbol{n=0}}^{\boldsymbol{N_{surf}}} \left(\frac{\partial \boldsymbol{J}}{\partial \boldsymbol{x_{S_n}}}\frac{\partial \boldsymbol{x_{S_n}}}{\partial \alpha_i} + \frac{\partial \boldsymbol{J}}{\partial \boldsymbol{y_{S_n}}}\frac{\partial \boldsymbol{y_{S_n}}}{\partial \alpha_i} + \frac{\partial \boldsymbol{J}}{\partial \boldsymbol{z_{S_n}}}\frac{\partial \boldsymbol{z_{S_n}}}{\partial \alpha_i}\right) \textbf{ for } \boldsymbol{i} = \boldsymbol{1}, \dots, \boldsymbol{N_\alpha} \tag{3.22}$$

where $\boldsymbol{N_\alpha}$ is the number of design variables and $\boldsymbol{N_{surf}}$ is the number of blade surface coordinates. Eventually, it is presented the design variables array, which includes each design variable's sensitivity:

$$\frac{\mathrm{d}\boldsymbol{J}}{\mathrm{d}\alpha} = \left(\frac{\mathrm{d}\boldsymbol{J}}{\mathrm{d}\boldsymbol{\alpha_1}}, \frac{\mathrm{d}\boldsymbol{J}}{\mathrm{d}\boldsymbol{\alpha_2}}, \dots, \frac{\mathrm{d}\boldsymbol{J}}{\mathrm{d}\boldsymbol{\alpha_{N_\alpha}}}\right) \tag{3.23}$$

3.5 Optimization

This is the process that closes the optimizer workflow. For this study, no numerical framework was coded in Python, as the whole procedure was carried out manually. SU2 provides a set of previously implemented constraint functions:

1. Entropy generation
2. Outlet total pressure
3. Outlet flow angle
4. Dimensionless power output

However, for this study, the constraint for the shape deformation was applied directly to the mesh deformation parametrization. Specifically, it was chosen to fix specific planes, preventing any displacement of the surface points – therefore the design variables connected to them – laying on those planes.

CHAPTER IV

TEST CASE

Here below, the test case is evaluated with the methodologies presented earlier. It consists of a full cascade, single passage, flow domain of a vaned centrifugal compressor. The fluid domain and respective geometries are property of MAN Energy Solution Schweiz AG that provided also the reference speedline data for the validation study.

4.1 Test case definition

Given that the aim of the study is to perform a multi-operating point adjoint optimization, the considered radial cascade is composed of three main zones (Fig.10):

1. Inlet channel
2. Impeller
3. Vaned Diffuser

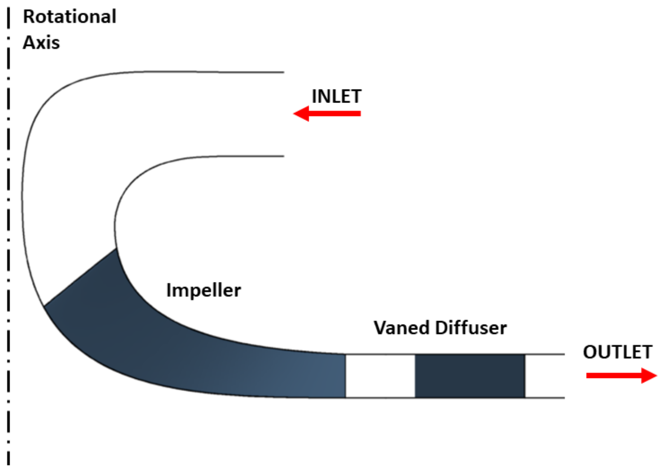

Figure 10: Test case meridian view.

The rotational axis imposed in in z direction. Please note that the impeller is shrouded, hence no tip gap modeling was required.

4.2 Domain discretization

The initial structure, multiblock, grid is generated by MAN Energy Solution Schweiz AG using NUMECA AutoGrid [29]. For the mesh towards close to the endwalls – e.g., hub, shroud and blade – $\boldsymbol{y^+ < 1}$ was imposed as mesh characteristic for the aforementioned areas. This operation is necessary considering that wall functions were not defined for this computational study. The grid consists of approximately 1.7 million elements (Fig 11).

Figure 11: Single passage, multiblock grid for the domain investigated.

From Figure 11 it is clearly noticeable the work done on the walls mentioned above in this section.

Being this a multizone case, different rotating frames were set for each of the zones specified in Fig.10. In the following table, the rotational speed for the mesh and each zone is specified.

Table 2: Domain zones and rotational speed imposed.

Inlet channel	Stationary
Impeller	Rotational
Vaned Diffuser	Stationary

4.3 Flow and adjoint solver

As mentioned in Chapter 3, SU2 CFD software is used to compute the flow field solution. Given the importance of viscous flow phenomena in turbomachinery application, the flow was modeled solving Reynolds-Averaged Navier Stokes equations. The second-order accurate Roe upwind scheme was chosen to discretize the convective fluxes. Initially, a first-order accurate solution was computed. Using the latter as an initialized flow field solution, a second-order accuracy was achieved with the MUSCL reconstruction. The mass flow rate imbalance between inlet and outlet dropped below 1% roughly after 9000 iterations and the solution was deemed to be converged (Fig. 12). Time discretization is obtained with and Euler implicit scheme, with a CFL number of 35 was imposed. Giles NRBC boundary conditions were set not only for inlet and outlet of the domain, but also for the mixing-planes interfaces. The respective values imposed for each surface can be found in Table 2. Please note that the inlet flow velocity was imposed to be normal to the boundary.

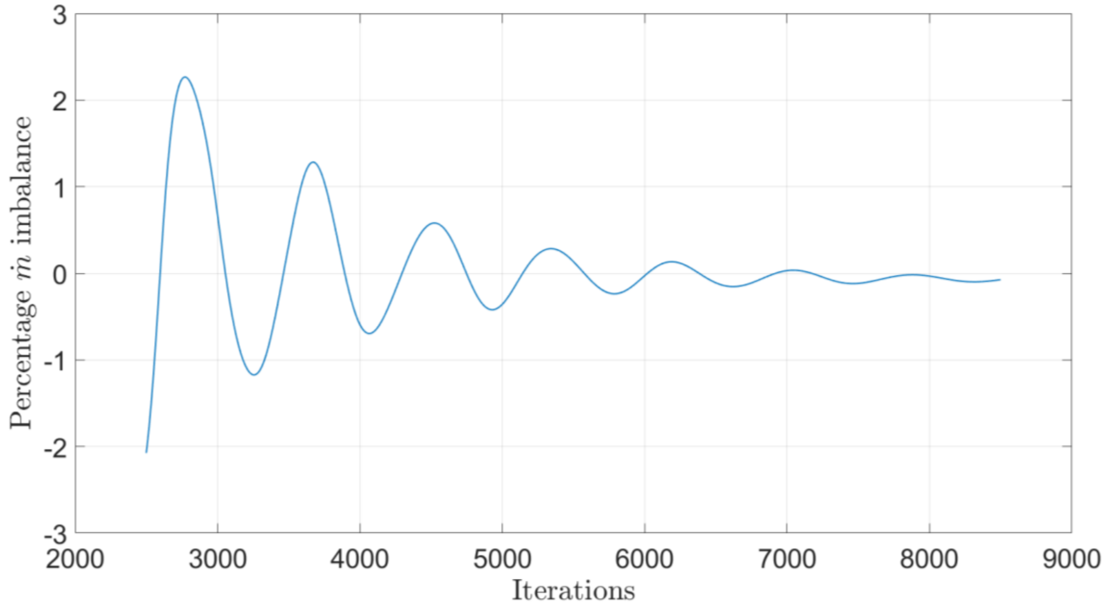

Figure 12: Mass flow imbalance of the flow solver solution.

Table 3: Boundary conditions imposed at inlet and outlet surfaces.

Inlet	Total Pressure [kPa] Total temperature [K]
Outlet	Static Pressure [kPa]

Endwalls surfaces were defined as adiabatic with no-slip condition. As mentioned above, only one flow passage is simulated, as SU2 code allows the imposition of periodic boundary conditions in circumferential directions. An overview of these settings can be visualized in Table 4 and Table 5.

Table 4: Boundary condition types

Inlet	**Outlet**	**Hub, shroud, blade**	**Periodics**
NRBC	NRBC	No-slip walls	1:1 Rot. periodicity

For steady or unsteady flow, the unphysical waves reflection at the far-field might be worsening the accuracy of the flow field simulation. Hence, non-reflective boundary conditions were imposed to ensure all the departing waves to exit the domain with no reflection [30]. Please note that the values imposed as boundary conditions at the inlet channel inflow surface and at the diffuser outlet surface were experimentally measured by MAN Energy Solutions Schweiz AG.

Table 5: Solver settings.

Conv. Scheme	**Time Disc.**	**Edge limiter**	**CFL number**
Roe	Euler Implicit	Van Albada Edge	35

Turbulence modeling is carried out utilizing the k-ω Shear-Stress-Transport (SST) turbulence model previously implemented in the software.

Please note that, by definition, the discrete adjoint numerical method inherits from the flow field solution its numerical properties. Hence, the same solver settings were applied to the adjoint solver.

4.4 Computational Performance

While discussing optimization problems, it is of fundamental importance to asses the computational performances for each SU2 module, with respect to different aspects (e.g. CPU-time, memory, resources, etc.). As mentioned in Section 4.3, a fully converged solution – for a single operating point – was obtained for the 1.7 million element grid in

8000 iterations (considering both first-order initialization and the second-order accurate reconstructed solution).

The computations were carried out using 8 cores Intel i7 7-12700H with 3.8 GHz clockspeed.

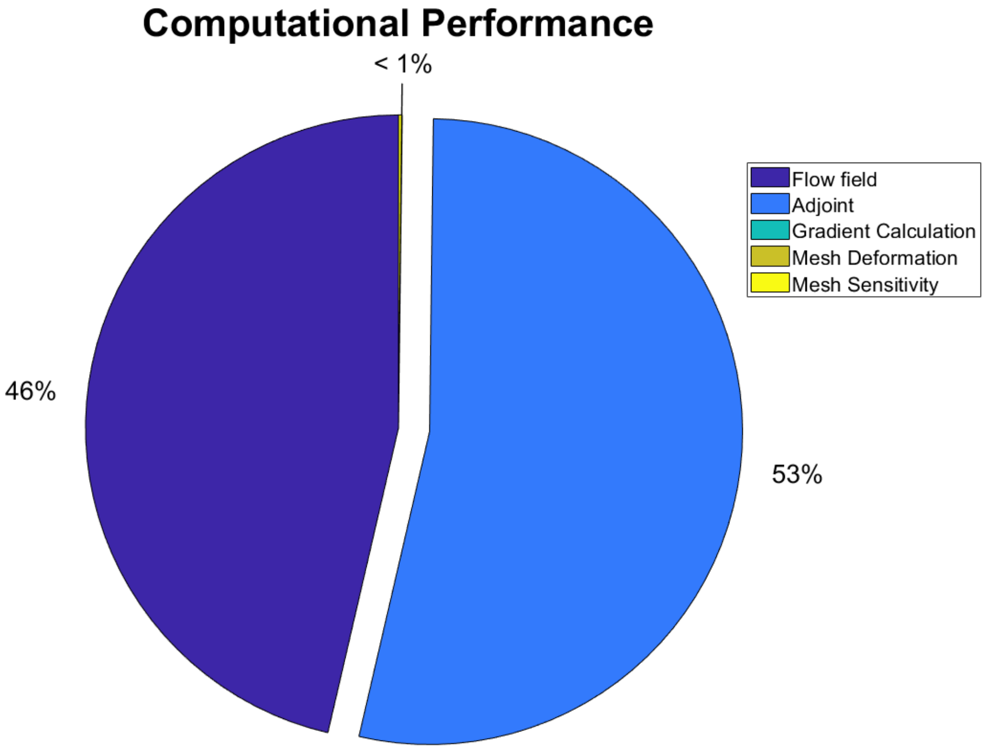

Figure 13: Computational performances evaluation.

The optimization for every operating point listed in Table 3, was obtained in 15870 minutes (equivalent to 265 hours, approximately 11 days). Given this data, utilization of High-Performance Computing (HPC) is mandatory.

To obtain the gradient through finite differences it is reasonable to expect exponentially higher computational cost. The benefits of the adjoint solver are easily understood from these considerations.

CHAPTER V

RESULTS AND DISCUSSION

Validation and optimization results for each test-case scenario are deeply analyzed. Particular focus is given to flow-phenomena and total pressure losses caused by the separation downstream of the vane leading edge. Moreover, a comparison with a single-point optimization study is also presented.

Eventually, a performance analysis is also carried out to highlight the difference between baseline and optimized design.

5.1 Viscous flow solution and its validation

Recalling what stated in Chapter 4, the single passage, flow domain was discretized using a third-party grid generator combining three different zones – inlet channel, impeller and vaned diffuser – for a total number of elements of 1.7 million. Table 5 summarizes the solver settings that were used for the numerical simulation. After the computation, SU2 results were compared with the reference speed line provided by MAN Energy Solution Schweiz AG – computed with the commercial software FidelityFlow – to carry out a validation of the baseline design. However, it is important to note that a previous, first-order accurate validation was already carried out (Uzuner et al., 2023).

To assess the validity of the obtained results, the baseline geometry was tested for twelve different operating points – from surging to choking conditions – to then compare its mass flow calculations, related to the outlet total pressure, with the reference data. In Fig.13 it is shown a good adherence of SU2 data with the reference solution.

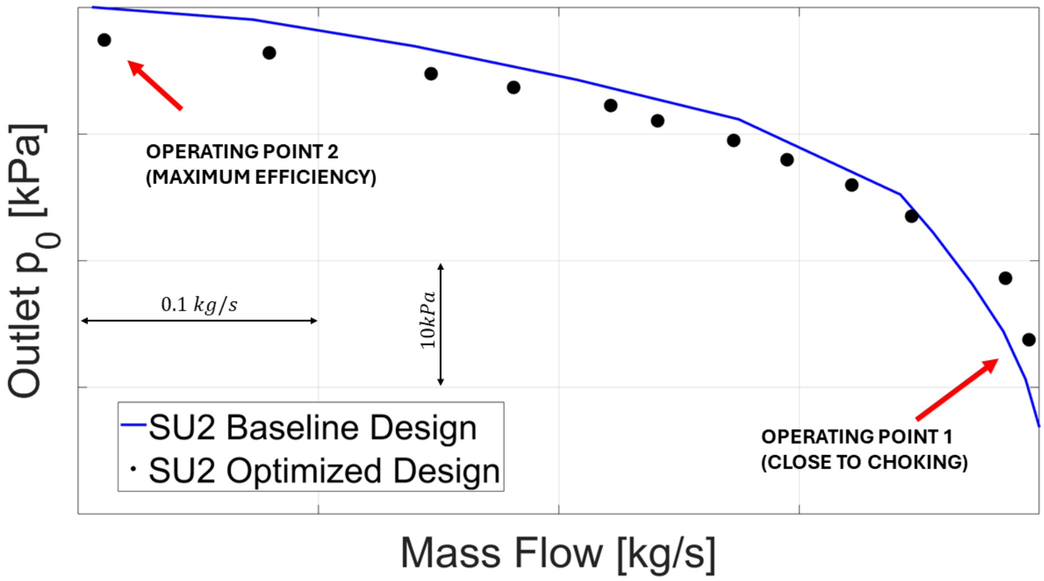

Figure 14: Compressor map traced by SU2 with respect to reference solution.

A second evaluation was performed with respect to efficiency values calculation. As visualized in Fig.14, SU2 can calculate the correct efficiency values with respect to the relative flow coefficient.

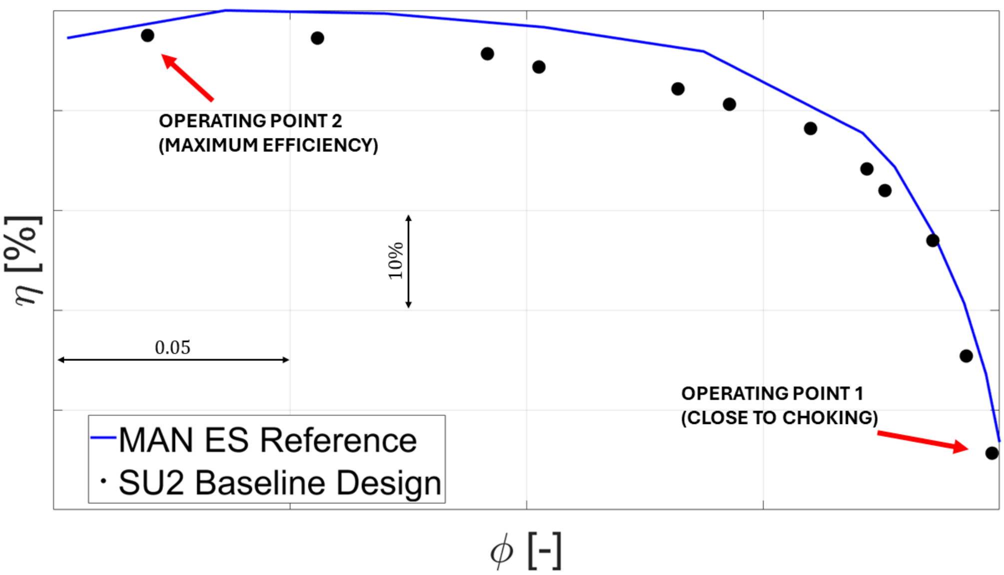

Figure 15: Efficiency comparison between SU2 data and reference solution.

Contextually, it is highlighted a slight deviation of these data – resulting in a few percentage points error – for some specific operating points. Please note that no numerical data about efficiency, mass flow rate and flow coefficient were disclosed, being this geometry protected by copyrights.

Moreover, a third assessment was carried out with respect to mixing plane boundary conditions to understand whether the numerical properties of each computational zone had been correctly transferred to the adjacent flow domain. For simplicity – due to the high number of simulations conducted to perform this study – only one comparison is presented in Table 3. However, it is intended that the same procedure was carried out for each simulation.

Table 6: Fluxes residual exponents between different zones of the computational domain for a single operating point.

Flux Relative Error	Inlet ch. – Impeller	Impeller - Diffuser
$\boldsymbol{\rho}$	-9.02	-8.94
$\boldsymbol{u_x}$	-6.53	-6.69
$\boldsymbol{u_y}$	-6.62	-6.57
$\boldsymbol{u_z}$	-6.82	-7.72
$\boldsymbol{k}$	-5.88	-5.33
$\boldsymbol{\omega}$	-2.83	-2.97

Table 6 shows that the mixing plane boundary conditions – briefly explained here above and implemented in Vitale et al., 2020 [28] – correctly conserves the fluxes residuals across the computational domain and its interfaces. The same publication referenced here above also shows the conservation of fluxes quantities along the spanwise direction. Considering that no further measurement uncertainty informations were provided, the presented results were estimated adequate bearing in mind the aim of this study.

Vaned diffusers are frequently used in centrifugal compressors because of the increased pressure recovery compared to vaneless diffusers. However, the performance of the vaned diffusers can dramatically deteriorate when the latter is subjected to excessive flow incidence. Fig. 16 shows the flow-field, at the midspan location, close to choking conditions. As shown by the streamline pattern, the flow incidence leads to a large separation zone at the suction side of the vane, which extends down to the trailing edge of the diffuser vane. The circulation pattern inside the separation zone and its viscous interaction with the surrounding flow is a major source of loss.

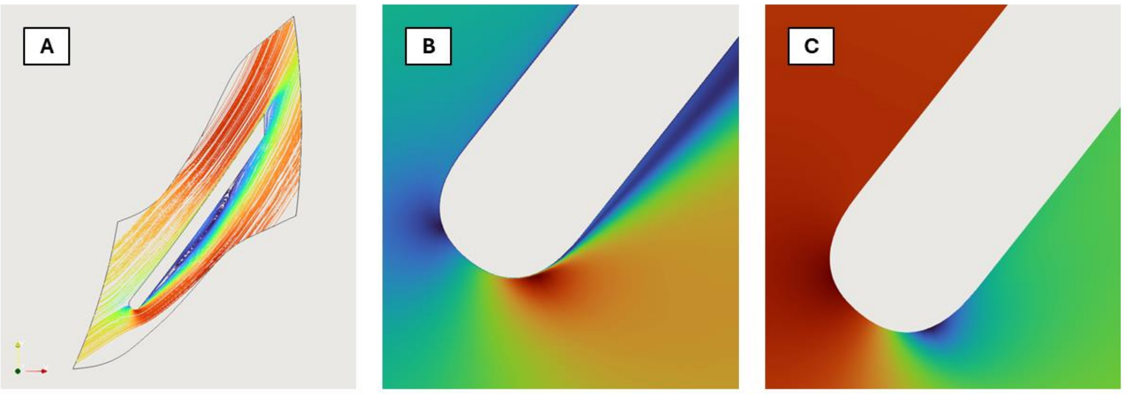

Figure 16: Vaned diffuser midspan section showing momentum streamlines and flow separation (A), Mach number contours (B) and static pressure contour (C) to highlight the critical source of losses in the machine, close to choking conditions.

Inversely, the flow-field at maximum efficiency operating point is presented here below. In Fig.7a it is possible to appreciate the difference in the flow conditions at almost zero incidence. The slightly negative incidence at the leading edge, shifts the location of the peak Mach number from the suction side to the pressure side of the diffuser vane. Also, the maximum Mach number value at the pressure side drops to 0.62. The lack of flow separation towards the leading edge reduces losses in comparison to the flow conditions close to choking (Fig.6).

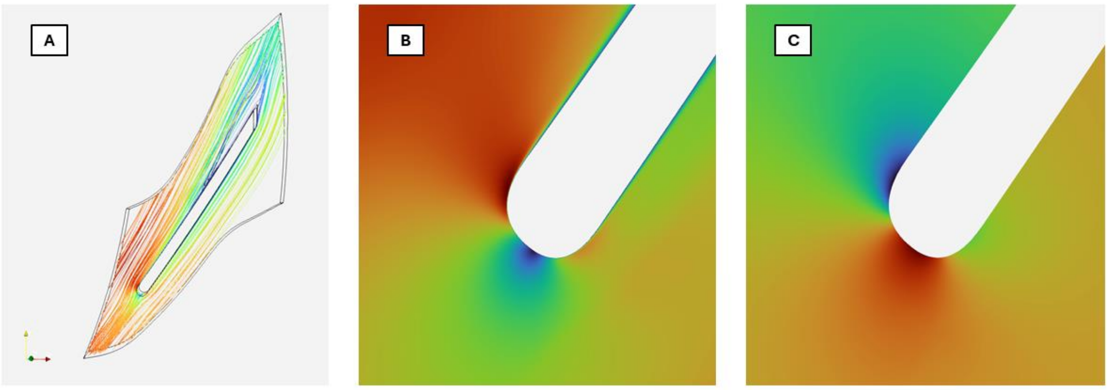

Figure 17: Vaned diffuser midspan section showing momentum streamlines and flow separation (A), Mach number contours (B) and static pressure contour (C) to highlight the critical source of losses in the machine, close to choking conditions.

The choking phenomenon described here above can be better visualized in Fig. 18, where the interaction between suction and pressure side of the vanes is displayed. It is possible to appreciate the transonic blockage downstream of the vanes leading-edge.

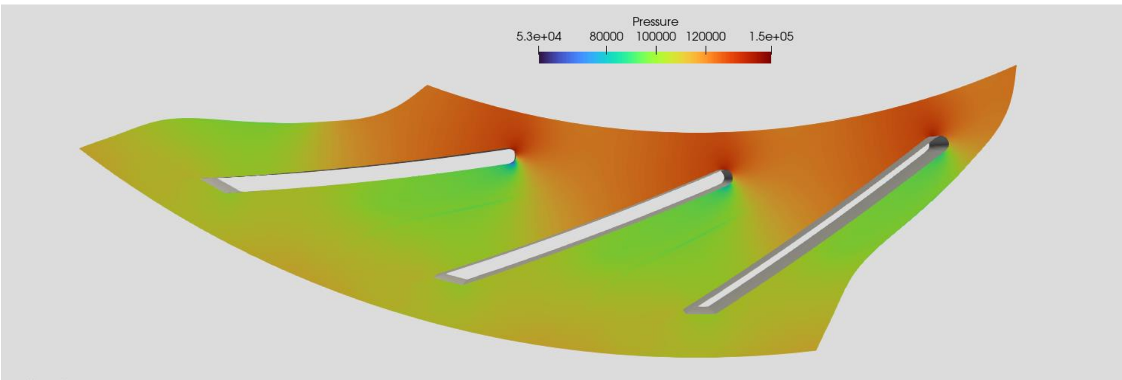

Figure 18: Triple-passage midspan pressure contour close to choking. conditions.

Given the domain streamlines and the contours presented in the previous paragraph (Fig.16) it is reasonable to say that flow separation is the governing phenomenon in the diffuser flow-field. For high flow rates, the increase of losses – and potentially the choking condition – are localized downstream of the leading-edge. After the diffuser throat, the entropy generation occurs in the boundary layer, increasing proportionally with the flow velocity. Consequently, to enhance the diffuser performances it is necessary to weaken the flow separation and reduce the transonic regime of the flow. Particular attention was given to the effects of the vane's leading-edge deformation with respect to the flow phenomena occurring in the domain. Consequently, it was chosen to optimize the vane with respect to this flow conditions. However, it is important to stress that single-point optimization in turbomachinery, indeed, could improve the performances of the single operating point itself, but the resulting geometry might also negatively affect the overall efficiency curve. Therefore, a second operating point was taken into account for the optimization, where the flow streamlines presented zero incidence on the diffuser vane (Fig.13, Fig.15).

5.2 Optimization set-up

Adjoint optimization – and consequently the shape deformation – were carried out specifically on the diffuser vane downstream of the impeller for the reasons specified in the introduction and in Section 5.1 of this chapter. The gradient combination – with respect to two different operating points – was mathematically formalized and numerically computed within the SU2 framework.

5.2.1 Objective Function Definition

As treated in Chapter 3 of this work, the objective function must be specified by the user. However, being this a multi-point optimization, it was necessary to customize the objective function to correctly calculate the total gradient. Specifically, losses within the diffuser domain are defined as follows:

$$Total\ Pressure\ Drop = P_{0|Diffuser\ Outlet} - P_{0|Diffuser\ Inlet} \qquad (5.01)$$

Hence, it was chosen to increase diffuser outlet total pressure as objective function for this study. However, while this could have been be sufficient for a single-point optimization, it was necessary to define an objective function that combines different diffuser outlet total pressure values, corresponding to each operating point, and its relative weighting coefficient as the compressor operational time is not the same for each operating point. Consequently, the objective function for the multi-point optimization was defined as follows:

$$J(x) = \sum_{i=1}^{2} \omega_i f_i(x) \quad \rightarrow \quad max \qquad (5.02)$$

where $f_i\ (x)$ is the diffuser outlet, area-averaged total pressure for the operating point i, ω_i is the weighting coefficient linked to the machine operational time and x is the FFD-box parameter.

5.2.2 Geometry Parametrization

The blade diffuser vane is parametrized with the FFD-box method discussed in Chapter 3. From Fig.19. it can be observed that the number of FFD control points it’s rather low compared to other studies carried out in the same field [28]. However, this choice was made as a primitive constraint for the shape deformation solver: allowing a deformation based on more control points would result in an unphysical new vane shape.

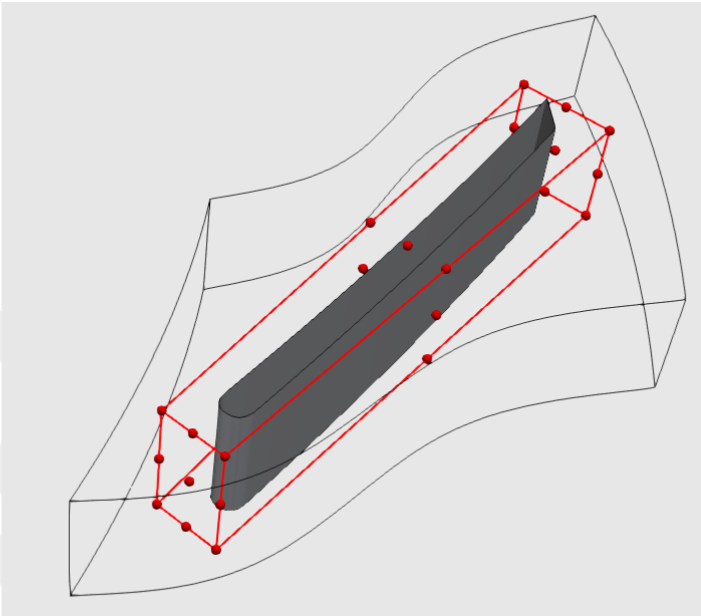

Figure 19: Visualization of the FFD-box and its control points.

Secondarily, one more constraint was applied: to the points laying on the hub and shroud planes, respectively, a position fixing was imposed. Hence, regardless of the gradient values calculated on those design variables, the mesh deformation displacement will always be zero. Overall, these settings (Table 6) allowed the solver to output a reasonable mesh deformation, resulting in a new design that could be easily industrialized.

Table 7: Shape parametrization settings.

Shape parametrization	**FFD degree**	**Plane fixing**
FFD-box	x-dir = 2 y-dir = 2 z-dir = 2	FFD_FIX_K = (2,0,0)

Please note that the trailing edge is included in the FFD-box domain. This was possible due to the constraints imposed here above, allowing a shape deformation along the whole blade.

5.2.3 Optimization convergence study

The optimization process took 5 design iterations to converge before the solver to outputs an optimized vane shape that, however, could not produce a positive increase in the total pressure loss. Moreover, unfeasible volumetric shapes were produced and the design was deemed not useful for the purpose of this study (Table 10).

Table 8: Mesh quality variation with respect to optimization design step.

Design Step	Mesh Quality
1	Good
2	Good
3	Good
4	Good
5	Negative volumes, overlapping surfaces, Outlet pressure not increasing

The difference between baseline and optimized design can be visualized in Fig. 20.

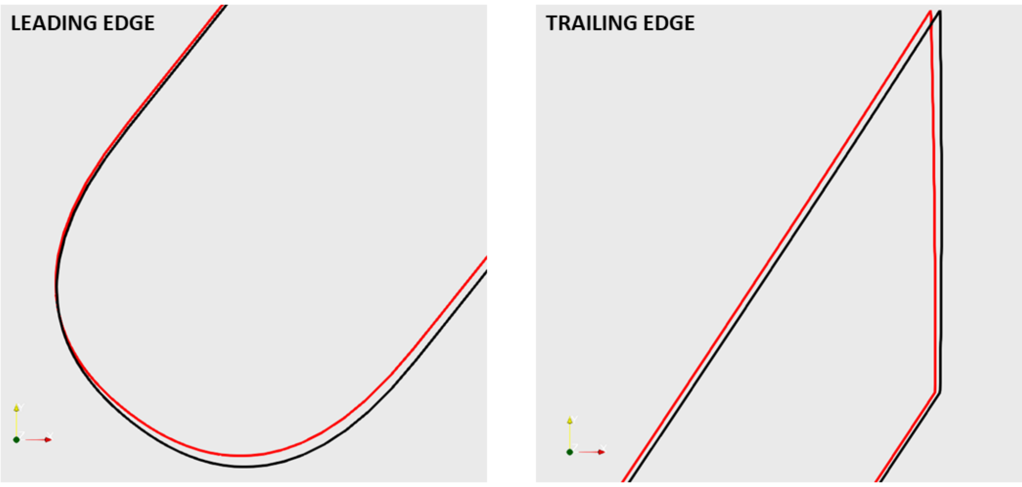

Figure 20: Midspan blade deformation comparison between baseline design (black) and optimized design (red).

The optimization process was considered converged after the first iteration that did not provide an outlet total pressure increase with respect to the baseline design or the previous optimized designs. While it might be argued that the convergence could not be monotone, it must be kept in consideration that the optimization workflow is to be intended for industrial applications, hence with some restrictions due to manufacturing issues. Further gradients calculations and shape deformations were investigated before considering the optimization cycle completed; however, none of the investigated geometry improved the performances more than the one presented in this paper, neither was deemed suitable for industrial production – therefore testing – given its extreme, sometimes unphysical, shapes generated by the FFD-box plane fixing removal to further extend the shape deformation otherwise impossible. Moreover, because the selected operating-points for the optimization are located towards opposite operating conditions, the gradients calculated for each of those are generating design variable's displacements in opposite directions, therefore reducing the whole mesh deformation. Specifically, this aspect could be observed in gradients with opposite sign.

5.3 Evaluation of the new design

Firstly, the results of the optimization for a single operating point are discussed. Next, the optimization study is repeated considering two different operating points: one at the best efficiency and the other at the lowest efficiency point that is observed being close to choking conditions. This gives the chance to better appreciate the difference between multi and single-operating point optimization and the effects that these two approaches have on the final performances of the machine. For the quantification of the performance difference between the baseline vane geometry and the optimized ones, the total pressure loss coefficient [31] is considered and the definition of such coefficient is given in Eq.6. In this definition the total and static pressure values are area averaged on the planes upstream and downstream of the diffuser vane.

$$Y = \frac{P_{01} - P_{02}}{P_{01} - P_1} \qquad (5.03)$$

The variation in the total pressure loss coefficient for both single-point and multi-point optimization are presented in Table 9 and Table 10. With this analysis, it is evident the significant, negative impact of the single operating point optimization for – at least – one different operating point along the same speedline (Table 9): the single-point optimization also led to an increase in loss for other operating conditions. On the other hand, the multi-operating point approach shows a less magnified loss decrement, however extended to the other operating conditions.

5.3.1 Multi-point optimization results

Given the domain streamlines (Fig.16) it is reasonable to say that flow separation and transonic flow are the two governing phenomena of the diffuser flow field. Consequently, to enhance the diffuser performances it is necessary to eliminate the flow separation and to reduce the blockage in the proximity of the diffuser throat. The vane shape deformation – even if kept minimal on purpose not to affect the overall speedline of the compressor – provided an optimized design with some marked differences if compared to the baseline blade profile. Specifically, the vane's leading edge seems converging to a more elliptical shape, while the trailing edge is slightly shifted; the metal angle is not constant with respect to spanwise location (Fig.22).

Table 9: Diffuser optimized design total pressure loss coefficient decrease with respect to baseline geometry.

Operating point	Baseline	Optimized
Close to choking	1.0892	1.0784
Maximum efficiency	0.1256	0.1247

Total pressure loss coefficients for the multipoint optimization are presented in Table 9. It is observed that the total pressure loss coefficient is higher than 1 close to choking conditions. This is traced back to the extreme off-design conditions the machine is operated at: PS and SS of the diffuser vane are switching location due to the high incidence with the flow direction. Moreover, the static pressure recovery in the diffuser is – for this operating point – negative. Because of energy conservation equation, this results in a total pressure loss coefficient higher than 1, suggesting that the diffuser is now acting like a nozzle. A detailed view of the pressure behavior previously described can be well visualized in Fig.21.

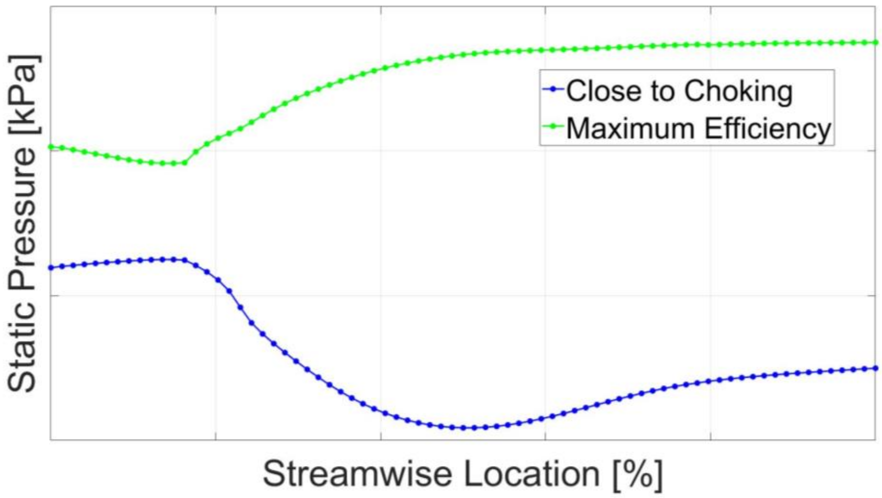

Figure 21: Static Pressure variation in the diffuser flow passage.

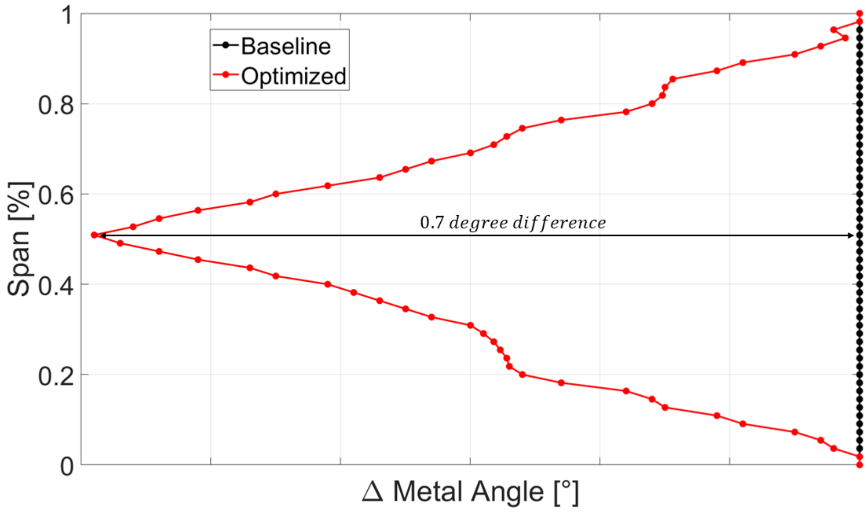

Figure 22: Baseline and optimized vane metal angles.

Considering the loss phenomena described in the previous section, the leading edge shape was modified to reduce the transonic regime of the flow occurring towards this region (Fig.17). On the other hand, the trailing edge shifting provided a reduction in the flow separation and in the mixing in the proximity of the diffuser exit. These shape deformations also lead to decrease in the entropy distribution at the diffuser outlet (Fig.22) where a marked reduction is observed close to choking conditions.

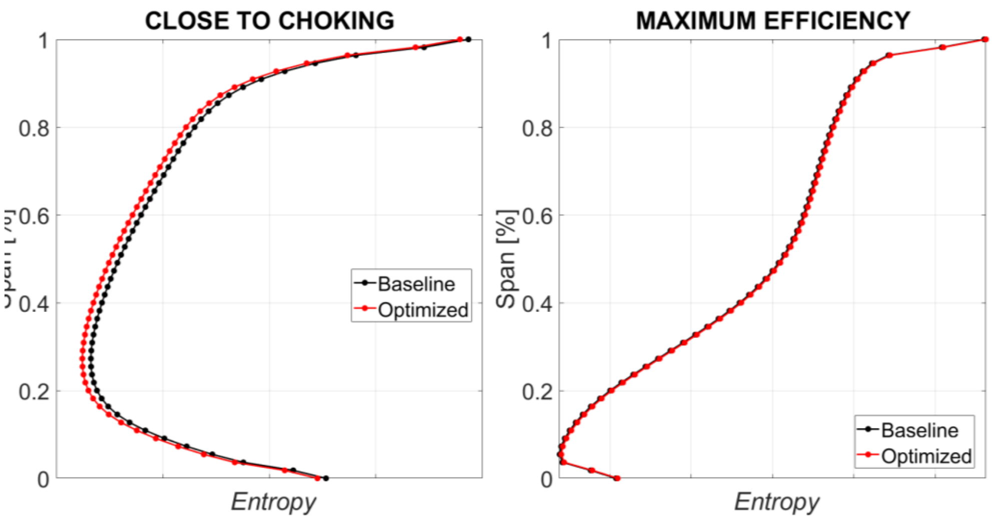

Figure 23: Entropy distribution at diffuser outlet.

5.3.2 Effect of the Diffuser Vane Optimization on the Compressor Performance

After the initial loss analysis conducted on the diffuser and presented in the previous section, the optimized design was post-processed to detect, if any, performance improvements for each operating point of the compressor map. It is crucial to observe that the gradient-based optimized design not only led to a performance enhancement for the selected operating points – respect to which the optimization study was carried out – but also magnified the efficiency along the whole operating range of the machine. The same results can be observed plotting the compressor map (Fig.23,24).

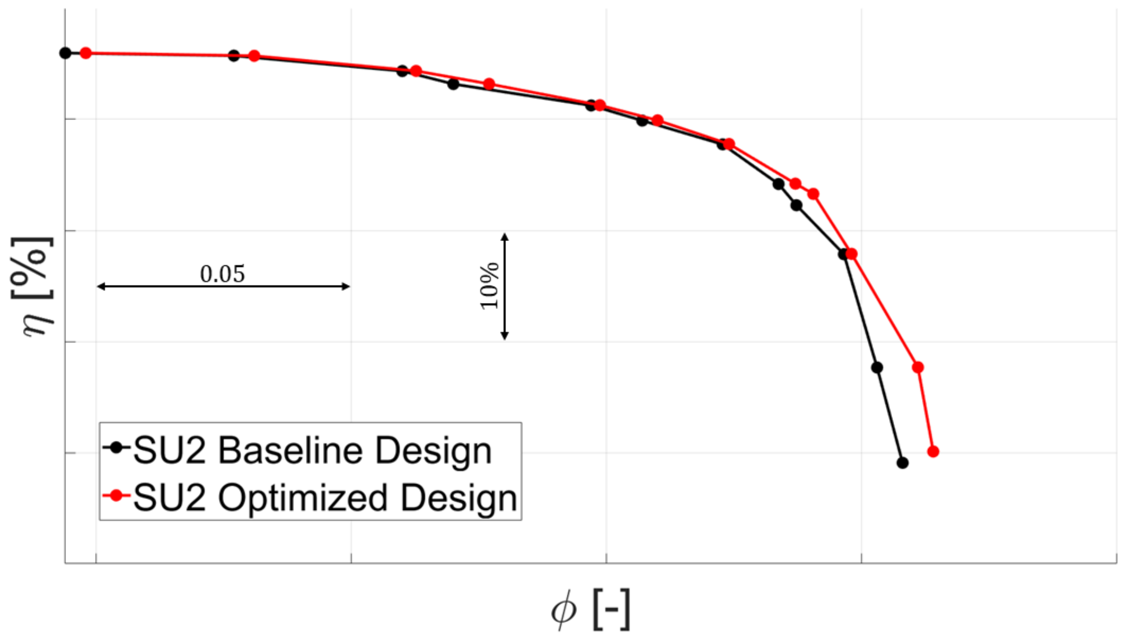

Figure 24: Comparison between baseline and optimized efficiency for each operating point.

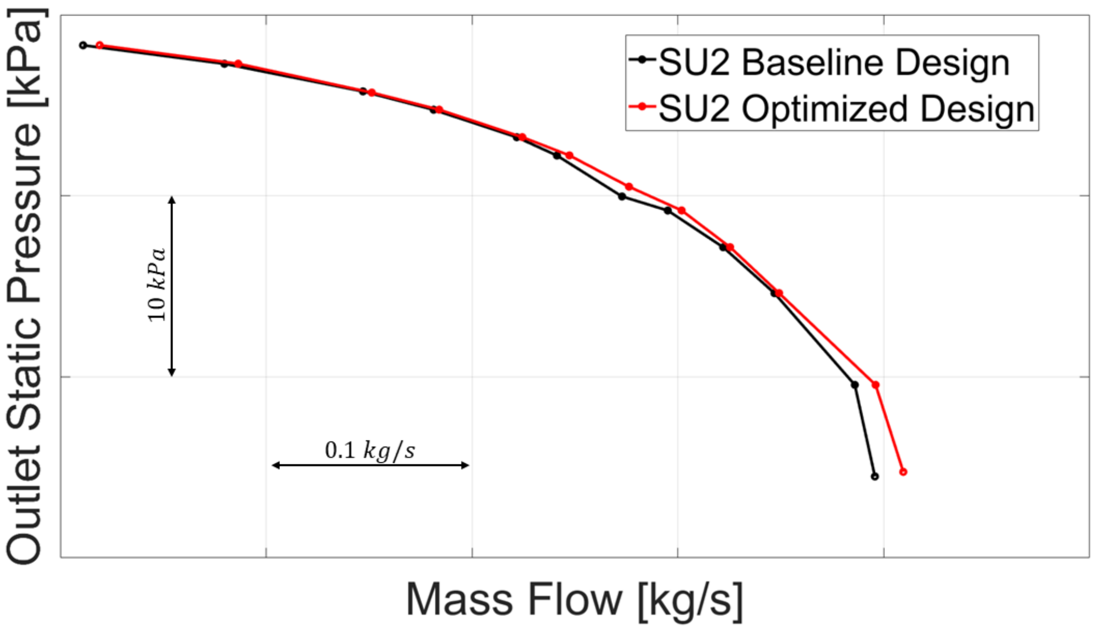

Figure 25: Baseline and optimized compressor map.

Referring to the optimized compressor map, it is observed a light shifting towards higher quantities of mass flow rate reaching its maximum towards chocking conditions where an improvement of 1.37% in the mass flow rate is registered. Similarly, a 1.99% increase in polytropic efficiency is registered for the same operating point mentioned here above. Moreover, Fig. 25 clearly shows the reduction in the flow separation – while operating the machine close to choking conditions (corresponding to operating point 12 in Fig.14) – towards the leading edge of the vane.

This aspect can be explained by recalling the shape deformation shown in Fig.20. The optimized design presents a reduced leading-edge radius, resulting in a smaller stagnation zone. Moreover, the leading-edge shape deformation positively affects the flow separation, resulting in a decreased flow separation area along the blade (Fig. 25).

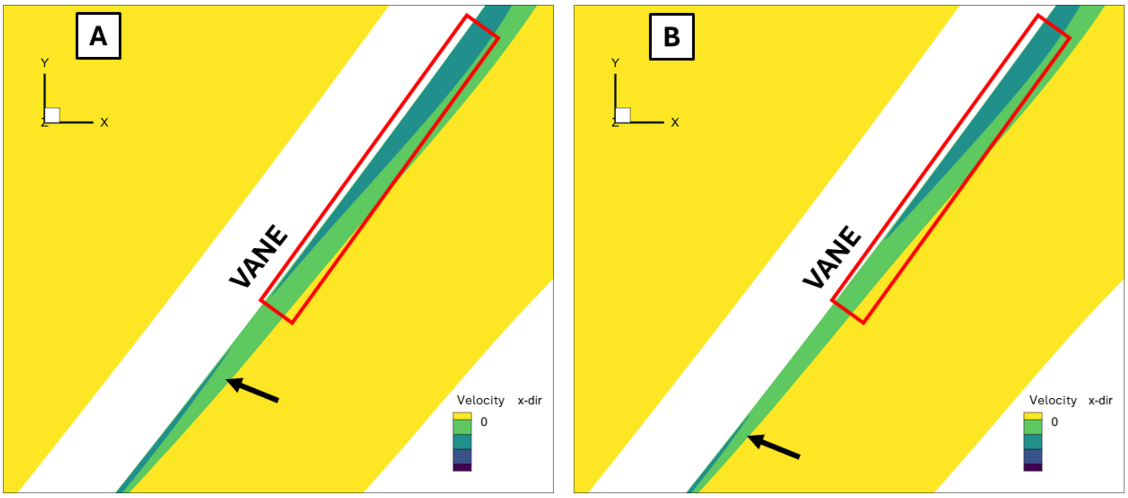

Figure 26: Flow separation region for baseline design (A) and optimized design (B) close to choking conditions.

5.4 *Comparison with single-point optimization approach*

To better appreciate the advantages of the multi-operating point optimization approach a single-point optimization study was also carried out on the same computational domain. Due to the weaker type of constraints applied to single-point optimization, the overall vane's shape deformation is much more extreme, especially at midspan (Fig. 26). While these results were not the eventual aim of this study, it was deemed important to present them in in detail to better express the effectiveness of the adjoint method.

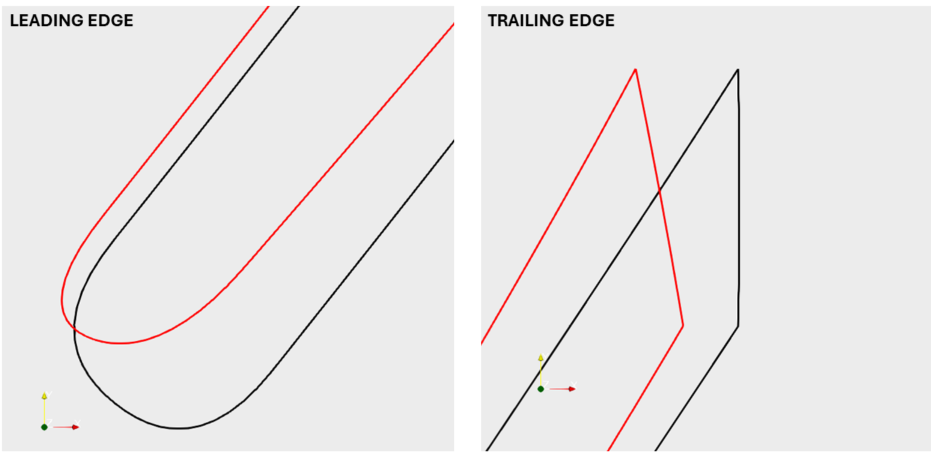

Figure 27: Midspan blade deformation for single-point optimization. Baseline design (black), optimized design (red).

The large separation area, generating towards the leading edge, is greatly reduced (Fig. 27). Consequently, a total pressure loss coefficient decrease is also registered. However, if the design presented in Fig.26 and Fig.27 was to be implemented for a different operating point other than the one it was explicitly optimized for – due to completely different incidence angle between the flow and the diffuser vane – the performances of the machine would be weakened (Tab.10).

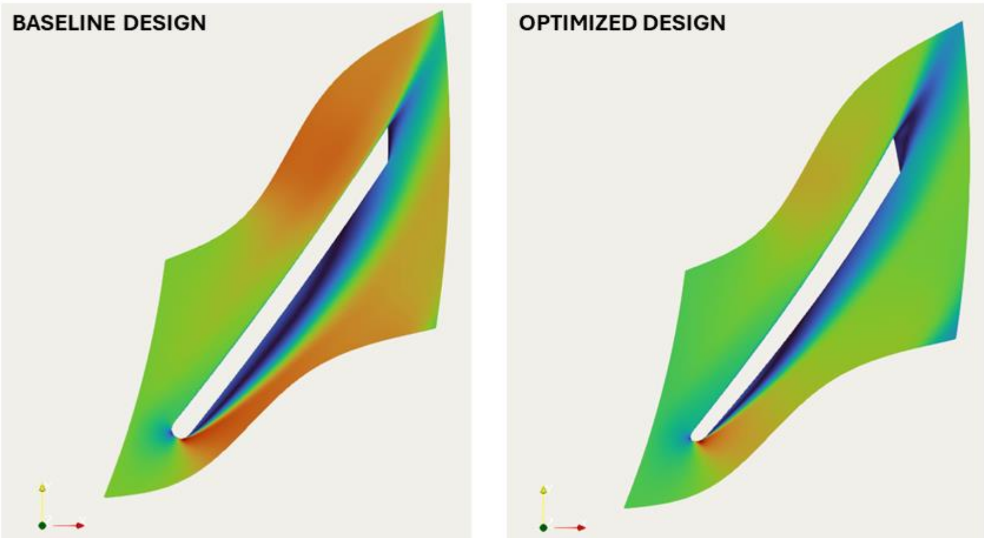

Figure 28: Midspan Mach number contour of baseline and optimized design with respect to a single operating point (close to choking conditions).

The single operating point optimization study was only conducted for the choking condition. The optimization process was kept on running while the total pressure at the diffuser outlet was increasing and stopped only when a drop in the total pressure was observed in consecutive iterations. (Fig.28).

Table 10: Diffuser optimized design total pressure loss coefficients with respect to baseline geometry for single-point optimization**.**

Operating point	Baseline	Optimized
Close to choking	1.0892	1.0431
Maximum Efficiency	0.1256	0.3452

Please note that the same convergence criteria were considered for the multi-point optimization study.

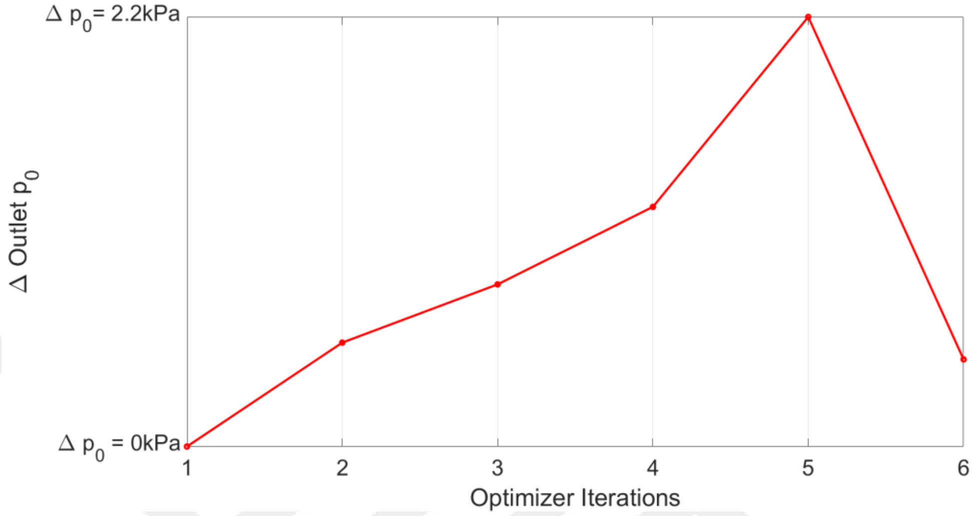

Figure 29: Adjoint single-point optimization convergence plot.

CHAPTER VI

CONCLUSIONS AND FUTURE PROSPECTS

Eventually, this chapter aims to summarize and highlight the contributions of this work and to suggest further recommendation for future research in the gradient-based turbomachinery optimization field.

The main objective of this work was to establish a multi-operating point, gradient-based optimization workflow for radial turbomachinery scenarios using SU2 open-source software. The novelty implemented is the multi-point objective function defined for the optimization, while this optimization process was widely carried out with respect to only a single operating point.

6.1 Conclusions

The main conclusions extrapolated from this work would correspond to the answer of the following main question that motivates this whole study:

Is it possible to establish a gradient-based optimization for turbomachinery scenarios with respect to multiple operating points of the machine itself?

The methodology that was studied and developed was successfully applied to the industrial test case: a full-cascade, single-passage ,centrifugal vaned diffuser designed by MAN Energy Solutions Schweiz AG.

The design variables gradients were successfully calculated by the solver and efficiently combined within the scope of the optimization process. Moreover, even though using

FFD-box shape parametrization for the diffuser vanes, the constraints applied to this method allowed to output an industrially feasible new vane design. The sensitivities and gradients computation accounted for 53% of the total computational time.

The original mesh, generated with boundary layer refinement for hub, shroud and blade surfaces, was efficiently deformed throughout the optimization process. No re-mesh steps were necessary as the constraint applied to the mesh deformation solver (SU2_DEF) allowed the grid to maintain its periodicity and structure. The mesh deformation only impacted for less than 1% on the total computational time. The convergency of the spring-analogy-based method for the grid modification always converged smoothly – given the number of elements of the grid tested – displaying a sufficient residuals reduction.

In conclusion, a process chain for the optimization of radial turbomachinery with respect to multiple operating points was successfully created. The geometrical constraints were efficiently imposed regardless of the shape parametrization method; the gradients computed using the adjoint method accurately define the correct optimization direction. Hence, even if operating with a fine grid, a good overall robustness was encountered.

6.2 Future work and recommendations

While the open-source software SU2 is of great stability when it comes to optimization set ups and automatic differentiation, further developments must be made to consent a smoother utilization of this powerful tool:

- Second-order accurate convective schemes always require a first-order solution to be initialized with. While theoretically this does not affect the workflow itself, it becomes of huge importance with respect to the computational cost evaluation, which is around 20/25%. Hence, more robustness of JST and Roe upwind scheme is required as their convergence rate is widely problem dependent.

- While the FFD-box shape parametrization method was deemed appropriate for this study, it might not be the case for radial turbomachinery impeller blades, given their shape intrinsically not coupling well with the shape of the FFD-box. Several CAD-based studies were carried out but a tool – implemented withing the SU2 suite framework – would be optimal for this kind of problem.

REFERENCES

[1] S. L. Dixon and C. A. Hall, *Fluid mechanics and thermodynamics of turbomachinery*. Kidlington, Oxford, Uk: Butterworth-Heinemann, 2014.

[2] T. D. Economon, F. Palacios, S. R. Copeland, T. W. Lukaczyk, and J. J. Alonso, "SU2: An Open-Source Suite for Multiphysics Simulation and Design," *AIAA Journal*, vol. 54, no. 3, pp. 828–846, Mar. 2016, doi: https://doi.org/10.2514/1.j053813.

[3] N. Anand, S. Vitale, M. Pini, and P. Colonna, "Assessment of FFD and CAD-based shape parametrization methods for adjoint-based turbomachinery shape optimization.," *Global Power and Propulsion Forum - Proceedings of 2018*, vol. 1, pp. 1-8, May 2018, doi:https://www.researchgate.net/publication/325070829_Assessment_of_FFD_and_CAD-based_shape_parametrization_methods_for_adjoint-based_turbomachinery_shape_optimization.

[4] H.-Y. Wu, F. Liu, and Her Mann Tsai, "Aerodynamic Design of Turbine Blades Using an Adjoint Equation Method," *43rd Aerospace Sciences and Meeting Exhibit*, vol.1, pp. 1-13, Jan. 2005, doi: https://doi.org/10.2514/6.2005-1006.

[5] A. Jaworski and Jens-Dominik Müller, "Toward Modular Multigrid Design Optimisation," *Lecture notes in computational science and engineering*, vol. 64, pp. 281–291, Jan. 2008, doi: https://doi.org/10.1007/978-3-540-68942-3_25.

[6] J. A. Samareh, "Survey of Shape Parameterization Techniques for High-Fidelity Multidisciplinary Shape Optimization," *AIAA Journal*, vol. 39, no. 5, pp. 877–884, May 2001, doi: https://doi.org/10.2514/2.1391.

[7] M. C. Duta, Shahrokh Shahpar, and M. B. Giles, "Turbomachinery Design Optimization Using Automatic Differentiated Adjoint Code," *ASME Turbo Expo 2007 Conference Proceedings*, vol. 6, pp. 435-1444, May 2007, doi: https://doi.org/10.1115/gt2007-28329.

[8] L. Lapoworth, "HYDRA-CFD: A Framework for Collaborative CFD Development," *International Conference on Scientific and Engineering Computation (IC-SEC)*, vol. 30, no. 1987, 2004, Available: https://www.researchgate.net/publication/316171819_HYDRA-CFD_A_Framework_for_Collaborative_CFD_Development

[9] D. X. Wang and L. He, "Adjoint Aerodynamic Design Optimization for Blades in Multistage Turbomachines—Part I: Methodology and Verification," *Journal of Turbomachinery*, vol. 132, no. 2, pp. 1-14, Apr. 2010, doi: https://doi.org/10.1115/1.3072498.

[10] D. X. Wang, L. He, Y. S. Li, and R. G. Wells, “Adjoint Aerodynamic Design Optimization for Blades in Multistage Turbomachines—Part II: Validation and Application,” *Journal of Turbomachinery*, vol. 132, no. 2, pp. 1-11, Apr. 2010, doi: https://doi.org/10.1115/1.3103928.

[11] S. Vitale, “Advancements in automated design methods for NICFD turbomachinery”, Doctoral Thesis, Nov. 2018, doi: https://doi.org/10.4233/uuid:a5efc9a0-0f9a-4ced-88be-51da26607ec0.

[12] S. Xu, D. Radford, M. Meyer, and Jens-Dominik Müller, “CAD-Based Adjoint Shape Optimisation of a One-Stage Turbine With Geometric Constraints,” *ASME Turbo Expo 2015 Conference Proceedings*, vol. 2C, pp. 1-14 Jun. 2015, doi: https://doi.org/10.1115/gt2015-42237.

[13] “OpenFOAM: The Open source CFD toolbox,” *www.openfoam.com*. https://www.openfoam.com

[14] “ANSYS Fluent Adjoint Solver,” *www.ansys.com*. https://www.ansys.com/products/fluids/

[15] B. Walther and S. Nadarajah, “Optimum Shape Design for Multirow Turbomachinery Configurations Using a Discrete Adjoint Approach and an Efficient Radial Basis Function Deformation Scheme for Complex Multiblock Grids,” *Journal of Turbomachinery*, vol. 137, no. 8, pp.1-20, Aug. 2015, doi: https://doi.org/10.1115/1.4029550.

[16] J. R. R. A. Martins, P. Sturdza, and J. J. Alonso, “The complex-step derivative approximation,” *ACM Transactions on Mathematical Software*, vol. 29, no. 3, pp. 245–262, Sep. 2003, doi: https://doi.org/10.1145/838250.838251.

[17] A. Jameson, “Aerodynamic design via control theory,” *Journal of Scientific Computing*, vol. 3, no. 3, pp. 233–260, Sep. 1988, doi: https://doi.org/10.1007/bf01061285.

[18] D. Papadimitriou and K. C. Giannakoglou, “Compressor Blade Optimization Using a Continuous Adjoint Formulation,” *ASME Turbo Expo 2006 Conference Proceedings*, vol. 6, pp. 1309-1317, May 2006, doi: https://doi.org/10.1115/gt2006-90466.

[19] M. B. Giles, M. C. Duta, Jens-Dominik Müller, and N. A. Pierce, “Algorithm Developments for Discrete Adjoint Methods,” *AIAA Journal*, vol. 41, no. 2, pp. 198–205, Feb. 2003, doi: https://doi.org/10.2514/2.1961.

[20] A. Rubino, “Reduced Order Models For Unsteady Fluid Dynamic Optimization of Turbomachinery”, Doctoral Thesis, Jul. 2019, doi: https://doi.org/10.4233/uuid:11bb7f0d-c39b-4a32-8936-6ff8905543e1.

[21] F. Palacios *et al.*, “Stanford University Unstructured (SU^2): An open-source integrated computational environment for multi-physics simulation and design,” *51st AIAA Aerospace Sciences Meeting including the New Horizons Forum and Aerospace Exposition*, vol. 287, pp. 1-60, Jan. 2013, doi: https://doi.org/10.2514/6.2013-287.

[22] P. SPALART and S. ALLMARAS, “A one-equation turbulence model for aerodynamic flows,” *30th Aerospace Sciences Meeting and Exhibit*, vol. 439, pp. 1-22, Jan. 1992, doi: https://doi.org/10.2514/6.1992-439.

[23] F. Menter, “Zonal Two Equation k-w Turbulence Models For Aerodynamic Flows,” *23rd Fluid Dynamics, Plasmadynamics, and Lasers Conference*, vol. 93, pp 1-21, Jul. 1993, doi: https://doi.org/10.2514/6.1993-2906.

[24] A. Jameson, “Origins and Further Development of the Jameson–Schmidt–Turkel Scheme,” *AIAA Journal*, vol. 55, no. 5, pp. 1487–1510, May 2017, doi: https://doi.org/10.2514/1.j055493.

[25] P. L. Roe, “Approximate Riemann solvers, parameter vectors, and difference schemes,” *Journal of Computational Physics*, vol. 43, no. 2, pp. 357–372, Oct. 1981, doi: https://doi.org/10.1016/0021-9991(81)90128-5.

[26] V. VENKATAKRISHNAN, “On the accuracy of limiters and convergence to steady state solutions,” *31st Aerospace Sciences Meeting*, vol. 880, pp. 1-10, Jan. 1993, doi: https://doi.org/10.2514/6.1993-880.

[27] G.D. van Albada, B. van Leer, and W. C. Roberts, “A Comparative Study of Computational Methods in Cosmic Gas Dynamics,” *Astronomy and Astrophysics*, vol. 108, pp. 95–103, Jan. 1997, doi: https://doi.org/10.1007/978-3-642-60543-7_6.

[28] S. Vitale, M. Pini, and P. Colonna, “Multistage Turbomachinery Design Using the Discrete Adjoint Method Within the Open-Source Software SU2,” *Journal of Propulsion and Power*, vol. 36, no. 3, pp. 465–478, May 2020, doi: https://doi.org/10.2514/1.b37685.

[29] NUMECA , “Products | Meshing Solutions,” *NUMECA Autogrid 5*. https://www.numeca.de/en/products-meshing-solutions/ (accessed Dec. 06, 2023).

[30] A. P. Saxer and M. B. Giles, “Quasi-three-dimensional nonreflecting boundary conditions for Euler equations calculations,” *Journal of Propulsion and Power*, vol. 9, no. 2, pp. 263–271, Mar. 1993, doi: https://doi.org/10.2514/3.23618.

[31] J. D. Denton, “The 1993 IGTI Scholar Lecture: Loss Mechanisms in Turbomachines”, *Journal of Turbomachinery*, vol. 9, no. 4, pp. 621-656, doi:https://doi.org/10.1115/1.2929299.

VITA

Academics

2024 M.Sc. in Mechanical Engineering, Özyeğin University, Istanbul (TR)

2021 B.Sc. in Industrial Engineering, Università degli Studi Guglielmo Marconi, Rome (IT)

Working experience

2021-2023 Teaching Assistant, Özyeğin University, Istanbul (TR)

2018-2021 Minority Owner, O'Caffè SAS di O'Caffè SRL, Vittorio Veneto (IT)

Lorenzo Fabris received his B.Sc. in 2021 while developing his career in industry with a thesis on biofuels utilization for aerodynamics engines utilizations in Guglielmo Marconi University (Rome, Italy). After leaving his occupation for the academic field, he continued his studies with a M.Sc. in Mechanical Engineering in Özyeğin University, specializing in Turbomachinery Computational Fluid Dynamics, numerical methods and gradient-based optimizations.